

Charge separation: From the topology of molecular electronic transitions to the dye/semiconductor interfacial energetics and kinetics

Thibaud Etienne^{a,†} and Mariachiara Pastore^{b,c,‡}

^a Institut Charles Gerhardt – CNRS and Université de Montpellier, Place Eugène Bataillon – 34095 Montpellier, France

^b Université de Lorraine – Nancy, Laboratoire de Physique et Chimie Théoriques, Boulevard des Aiguillettes, 54506 Vandoeuvre-lès-Nancy, France

^c CNRS – Laboratoire de Physique et Chimie Théoriques, Boulevard des Aiguillettes, 54506 Vandoeuvre-lès-Nancy, France

† thibaud.etienne@umontpellier.fr

‡ mariachiara.pastore@univ-lorraine.fr

Abstract Charge separation properties, that is the ability of a chromophore, or a chromophore/semiconductor interface, to separate charges upon light absorption, are crucial characteristics for an efficient photovoltaic device. Starting from this concept, we devote the first part of this book chapter to the topological analysis of molecular electronic transitions induced by photon capture. Such analysis can be either qualitative or quantitative, and is presented here in the framework of the reduced density matrix theory applied to single-reference, multiconfigurational excited states. The qualitative strategies are separated into density-based and wave function-based approaches, while the quantitative methods reported here for analysing the photoinduced charge transfer nature are either fragment-based, global or statistical. In the second part of this chapter we extend the analysis to dye-sensitized metal oxide surface models, discussing interfacial charge separation, energetics and electron injection kinetics from the dye excited state to the semiconductor conduction band states.

Keywords Photoactivity; Excited States; Topology; Dye-sensitized metal oxides; Charge transfer; Injection rates.

1 Introduction

In the context of solar energy exploitation, dye-sensitized solar cells (DSCs)^{1–3} and dye-sensitized photoelectrosynthetic cells (DSPECs)^{4–7} offer the promise of cost effective sunlight conversion and storage, respectively. Since the seminal paper by O'Regan and Grätzel in 1991,⁸ hybrid/organic photovoltaic devices have attracted significant research interest, with the recent launch of the first commercial product. The heart of a *n*-type DSC is the photoanode, where a mesoporous oxide layer, usually TiO₂ or ZnO, is sensitized by a monolayer of dyes, chemically bound to the semiconductor nanoparticles. Upon solar irradiation, the adsorbed sensitizers are able to inject the photoexcited electrons in the manifold of the conduction band (CB) states of the semiconductor, typically at the femtosecond time scale. Injected electrons travel through the mesoporous film and are collected by the conductive layer of the photoanode electrode, while the oxidized dye is rapidly reduced by the electron mediator donor in solution or by the hole transporting material (HTM) in solid-state devices. The collected electrons flow in the external circuit, producing a photocurrent, and reach the counter-electrode, where the circuit is closed by the reduction of the electron mediator acceptor. Alternatively, in a *p*-type DSC, the photoactive electrode is a dye-functionalized nanostructured wide band gap *p*-type semiconductor (usually NiO).^{9–12} In this case the functioning mechanism is inverse, with hole injection from the photoexcited dye to the *p*-type semiconductor valence band (VB) and the concomitant electron transfer to the redox mediator and final electron collection at the anode.

Therefore, the key-phenomena at the center of the electron current photogeneration in DSCs are light-matter interaction and the subsequent intramolecular and interfacial charge separation.^{13,14} Indeed, when a molecule catches the light, it sees its electronic structure totally reorganized. While approaching theoretically the electronic structure of complex molecular systems is already quite a challenge,^{15,16} providing a reliable prediction about its time evolution due to the photoactivity of the molecule constitutes an arduous task.^{17,18} The keys to a proper description of the light-induced electronic cloud polarization are contained into the so-called exciton wave function, and several tools exist for unraveling the nature of molecular excited states, based the exciton analysis.^{19–27} Using the reduced density matrix theory for extracting and analyzing this information has already been proved to be of interest to theoretical and computational communities,^{28,29} but also in more applied research fields,^{30–33} and in particular in the DSCs community.^{34–38} Indeed, some strategies have already been developed for providing qualitative and quantitative insights into the topology of molecular electronic transitions with the projection of the exciton wave function in a finite-dimensional vector space (the transition density matrix^{20,28,39–50}) as a starting point.^{20,29} The most common approaches consist in constructing two one-particle wave functions (occupied/virtual Natural Transition Orbitals^{28,39–43}) or charge density functions (detachment/attachment densities^{41,51,52}) which allow for a straightforward perspective of the photo-induced electronic structure reorganization.^{20,29} A quantitative probing of the exciton locality, nature and structure, has also been derived.^{25,27,29,45,46,53–61}

The first part of this book chapter is devoted to the description of the mathematical details of the strategies established for assessing the locality and nature of molecular electronic transitions, as the knowledge about the potentiality of a molecule to separate charge in space is obviously extremely helpful when designing new dyes for solar cells applications. The second part discusses how the intramolecular charge separation (electronic structure and excited state properties) of the dye affects the interfacial energetics and overall charge generation characteristics of dye-sensitized photoelectrode models. We will start by investigating the “perturbation” of the dye and semiconductor energy levels due to the dye chemisorption on the TiO₂^{13,62} and NiO⁶³ surfaces to then move to the modelling of the dye and semiconductor electronic coupling and charge injection as a function of the dye molecular structure and substrate protonation.⁶⁴

2 Topology of molecular electronic transitions

In this section we will revisit various qualitative and quantitative tools for analyzing the charge displacement occurring upon light absorption, i.e., the electronic structure reorganization induced by the capture of a photon. While qualitative analyses provide visualization tools for assessing the nature of a charge transfer, the quantitative approaches consist of numbers that can be regarded as a collection of data for numerical analyses of the electronic transition character. Among the different approaches considered in this chapter, we can split the qualitative strategies into two parts: Those involving the analysis of charge density functions constructed from one-particle reduced density matrices of different nature, and those involving the analysis or the production of wave functions. For the quantitative counterpart, one can also consider two sets of mathematical objects: The fragment-based and the global strategies. While the former will provide charge transfer or excitation numbers that will be system-dependent (more exactly, they will depend on how the whole electronic system is divided into fragments according to the molecular structure), the latter produce numbers that represent the whole molecular system and its electronic structure. They are said to be “systematic” due to the fact that they target the entire, unfragmented system.

The choice of density or wave functions for the qualitative analysis of charge transfers can also be guided by the choice of the quantitative analysis to be used afterward, since for instance some quantitative insights can be derived from the singular values corresponding to natural transition orbitals (*vide infra*) while the hole/particle spatial overlap integral or the charge transfer integral can be computed more directly from detachment/attachment density functions (*vide infra*).

Note that for the sake of simplicity, through this section we will only depict the analysis of the outcome of calculations of electronic transitions between a single-reference electronic ground state and an excited state constructed as a linear combination of singly-excited Slater determinants (unless the contrary is explicitly stated).

Note finally that most of the features reported in this section can be found in software packages freely available on the web⁶⁵⁻⁶⁸

2.1 Background - State density matrix and charge density

As briefly recalled in Refs.^{28,29} to a quantum electronic state $|\psi_m\rangle$, projected in a spin-spatial space $\{\mathbf{x}\}$ where \mathbf{x} collects spatial (\mathbf{r}) and spin (σ) coordinates of the N electrons of a molecular system, i.e.,

$$|\psi_m\rangle \leftrightarrow \psi_m(\mathbf{x}) = \langle \mathbf{x} | \psi_m \rangle, \quad (1)$$

corresponds a reduced one-particle density matrix kernel $\tilde{\gamma}_m$

$$\tilde{\gamma}_m(\mathbf{r}_1; \mathbf{r}'_1) = N \sum_{\sigma_1=\alpha,\beta} \int d\mathbf{x}_2 \dots \int d\mathbf{x}_N \psi_m(\mathbf{r}_1, \sigma_1, \dots, \mathbf{x}_N) \psi_m^*(\mathbf{r}'_1, \sigma_1, \dots, \mathbf{x}_N). \quad (2)$$

When the wave function is expressed in the basis of L one-particle functions (spinorbitals - SOs) $\{\varphi\}$, with N of them being occupied, and $L - N$ unoccupied (virtual), $\tilde{\gamma}_m$ can be rewritten

$$\tilde{\gamma}_m(\mathbf{r}_1; \mathbf{r}'_1) = \sum_{r,s=1}^L \varphi_r(\mathbf{r}_1) (\gamma_m)_{rs} \varphi_s^*(\mathbf{r}'_1) \quad ; \quad (\gamma_m)_{rs} = \langle \psi_m | \hat{r}^\dagger \hat{s} | \psi_m \rangle \quad (3)$$

where γ_m is simply termed one-particle reduced density matrix (1-RDM). The \hat{r}^\dagger and \hat{s} operators are respectively the creation and annihilation operators from the second quantization. From the expression of $\tilde{\gamma}_m$ we see that the one-particle charge density (1-CD) for the quantum state $|\psi_m\rangle$ is the trace of $\tilde{\gamma}_m$

$$\tilde{\gamma}_m(\mathbf{r}_1; \mathbf{r}'_1) = n_m(\mathbf{r}_1) \quad \forall \mathbf{r}_1 = \mathbf{r}'_1. \quad (4)$$

We therefore see that for a given $\{\varphi\}$ basis, there is an unequivocal relationship between any 1-RDM and the corresponding 1-CD

$$\boldsymbol{\gamma} \xrightarrow{\mathbb{R}^3} n(\mathbf{r}_1) = \sum_{r,s=1}^L \varphi_r(\mathbf{r}_1) (\boldsymbol{\gamma})_{rs} \varphi_s^*(\mathbf{r}_1). \quad (5)$$

Since the outcome of the post-processing of electronic excited states quantum chemical calculations (or the outcome of the calculations themselves) is often a 1-RDM, this relationship will often be used for projecting a density matrix into the Euclidean space for visualizing changes in the charge density. Such type of analysis will be the basis for several qualitative analyses of photoinduced electronic structure reorganization, as introduced in the next paragraph.

2.2 Qualitative analysis of photoinduced electronic structure reorganization

As previously stated, we will first expose the direct use or the transformation of state density matrices for visualizing the photoinduced charge density rearrangement using one-particle density functions (charge densities or wave functions). We will first expose qualitative topological analyses involving 1-CD functions. Note that from now on, when two position coordinate vectors, \mathbf{r}_1 and \mathbf{r}'_1 , will be present in the expression of any function, these coordinates will respectively point to the hole and the particle generated by photon capture, similar to \mathbf{r} and \mathbf{r}' or \mathbf{r}_h and \mathbf{r}_e that one can meet in the literature.²⁰

2.2.1 Density-based strategies

As an outcome of an excited state quantum-chemical calculation, one obtains the 1-RDM of the ground ($\boldsymbol{\gamma}_0$) and the x^{th} excited state ($\boldsymbol{\gamma}_x$), together with the so-called one-particle transition density matrix (1-TDM, $\boldsymbol{\gamma}^{0x}$). These three matrices are the result of the projection of a reduced one-particle (transition) density matrix kernel into a finite SO space $\{\varphi\}$ (*vide supra*).

State densities

According to equation 5, one can obtain the projection of γ_0 and γ_x into the direct (Euclidean) space. Due to the linearity of such projection, it is also possible to unequivocally derive the 1-CD corresponding to the net change in the electron density between the excited and ground state from the difference of the state density matrices:

$$\gamma_x - \gamma_0 = \gamma^\Delta \xrightarrow{\mathbb{R}^3} n_\Delta(\mathbf{r}_1) = n_x(\mathbf{r}_1) - n_0(\mathbf{r}_1). \quad (6)$$

The so-called difference density, i.e., the difference between the 1-CD of the excited and ground states, can be used as a visualization tool to qualitatively locate the zones of space where the fluctuation of charge density is negative or positive. Two 1-CD functions ($n_\pm(\mathbf{r}_1)$) can then be written, based on the sign of the difference density everywhere in \mathbb{R}^3 , as⁵⁴

$$\frac{1}{2} \left\{ \sqrt{n_\Delta^2(\mathbf{r}_1) \pm n_\Delta(\mathbf{r}_1)} \right\} = n_\pm(\mathbf{r}_1) \in \mathbb{R}^+ \quad (7)$$

where we see that while the difference density can take positive or negative values, n_+ and n_- are both positive functions where they are not vanishing. One can therefore separate the positive and the absolute value of the negative contributions to the difference density by using the n_\pm function. Note that n_+ and n_- are two 1-CD functions with strictly no spatial overlap.

Charge displacement analysis

It is possible, through the so-called Excited State Charge Displacement (ESCD) analysis,^{69,70} to obtain a function along one coordinate (for example, z) which gives an idea of the charge displacement profile related to the transition between the ground and the excited states, along a molecular axis:

$$\Delta q^{0x}(z) = \int_{-\infty}^z dz' \int_{-\infty}^{+\infty} dx \int_{-\infty}^{+\infty} dy n_\Delta(x, y, z'). \quad (8)$$

This type of analysis is quite general, and will also be used in another context (*vide infra*) than the passage from ground to excited states.

Detachment/attachment densities

While the n_\pm functions correspond to the net increase/decrease of charge density through space, one can also be interested in visualizing the hole and the particle density through two 1-CD functions, termed “detachment” and “attachment” densities.^{41,51,52} For constructing these two functions, one has first to diagonalize the difference density matrix and, as for the n_\pm function in the Euclidean space, to use a \mathbf{k}_\pm matrix function in order to split the eigenvalues into two matrices according to their sign:

$$\exists (\mathbf{M}, \mathbf{k}_\pm) \mid \mathbf{M}^\dagger \gamma^\Delta \mathbf{M} = \mathbf{m}, \quad \mathbf{k}_\pm = \frac{1}{2} \left\{ \sqrt{\mathbf{m}^2 \pm \mathbf{m}} \right\}. \quad (9)$$

Backtransforming the resulting diagonal matrices returns the detachment (γ^d) and attachment (γ^a) 1-RDM, that can be projected into the direct space (see equation 5)

$$\mathbf{M} \mathbf{k}_- \mathbf{M}^\dagger = \gamma^d \xrightarrow{\mathbb{R}^3} n_d(\mathbf{r}_1) \quad ; \quad \mathbf{M} \mathbf{k}_+ \mathbf{M}^\dagger = \gamma^a \xrightarrow{\mathbb{R}^3} n_a(\mathbf{r}_1). \quad (10)$$

A quick look at these two 1-CD functions provides a clear idea of the location of the depletion/increment zones of electron density, generated by photon absorption (or emission). Note that unlike the n_\pm functions, the detachment/attachment densities can overlap (see the top of Figure 2 in Ref.²⁹). This spatial overlap can even be quantified (*vide infra*) and constitutes a measure of the exciton (i.e., the electron/hole pair) locality.

Transition densities

As in the case of the 1-RDM kernel, one can write a one-particle reduced *transition* density matrix kernel,^{20,28,29} where we find that the product of a state wave function by its complex conjugate is replaced by the product of a state wave function by the complex conjugate of the wave function corresponding to another quantum electronic state:

$$\tilde{\gamma}^{0x}(\mathbf{r}_1; \mathbf{r}'_1) = N \sum_{\sigma_1=\alpha,\beta} \int d\mathbf{x}_2 \dots \int d\mathbf{x}_N \psi_0(\mathbf{r}_1, \sigma_1, \dots, \mathbf{x}_N) \psi_x^*(\mathbf{r}'_1, \sigma_1, \dots, \mathbf{x}_N) \quad (11)$$

$$= z_x^{-1/2} \sum_{r,s=1}^L \varphi_r(\mathbf{r}_1) (\gamma^{0x})_{rs} \varphi_s^*(\mathbf{r}'_1). \quad (12)$$

where $z_x^{-1/2}$ is a normalization factor (*vide infra*). Here, we see that the couple of coordinates (\mathbf{r}_1 and \mathbf{r}'_1) is taken so that the hole (\mathbf{r}_1) originates from the ground state and the particle (\mathbf{r}'_1) belongs to the excited electronic state. This convention (\mathbf{r}_1 coordinates for the hole, \mathbf{r}'_1 for the particle) will be used through this book chapter. As in the case of state densities, the one-particle transition density function can be deduced from the kernel expression, and there is an unequivocal relation between the 1-TDM $z_x^{-1/2} \gamma^{0x}$ and the transition density

$$\tilde{\gamma}^{0x}(\mathbf{r}_1; \mathbf{r}'_1) = n_{0x}(\mathbf{r}_1) \forall \mathbf{r}_1 = \mathbf{r}'_1 \quad \Rightarrow \quad z_x^{-1/2} \gamma^{0x} \xrightarrow{\mathbb{R}^3} n_{0x}(\mathbf{r}_1) \quad (13)$$

Considering the 1-TDM kernel as the exciton wave function, one can use its trace to visualize the transition density and use it for evaluating transition properties.

2.2.2 Wave function-based strategies

Another possibility for visualizing the changes in the electronic structure of a molecule due to the capture of a photon is the use of one-particle wave functions (orbitals). Since the 1-TDM is given in the space of spinorbitals, one can interpret it as a compilation of the pondering coefficients describing an excited state as a superposition of single excitations from occupied to virtual spinorbitals, as explained below.

Spinorbitals (SOs) analysis

If an excited state $|\psi_x\rangle$ can be written as a linear combination of singly-excited Slater determinants

$$|\psi_x\rangle = \sum_{i=1}^N \sum_{a=N+1}^L z_x^{-1/2} (\gamma^{0x})_{ia} |\psi_i^a\rangle \quad ; \quad |\psi_i^a\rangle = \hat{a}^\dagger \hat{i} |\psi_0\rangle \quad (14)$$

with

$$z_x = \text{tr}(\gamma^{0x} \gamma^{0x\dagger}) = \text{tr}(\gamma^{0x\dagger} \gamma^{0x}), \quad (15)$$

then the 1-TDM elements can be seen as the coefficients corresponding to these singly-excited Slater determinants in the expression of the total excited state

$$\varphi_i \xrightarrow{z_x^{-1/2} (\gamma^{0x})_{ia}} \varphi_i \quad 1 \leq i \leq N < a \leq L \quad (16)$$

and one can split the total spinorbital space into two parts (occupied - i indices - and virtual - a indices) and pair the occupied (φ_i) and virtual (φ_a) spinorbitals according to the coefficients $z_x^{-1/2} (\gamma^{0x})_{ia}$ corresponding to each couple, so the electronic transition can be pictured as a linear combination of hole-to-particle ($1h1p$) contributions, with a total of one electron promoted from the ground to the excited state if we are in the above-mentioned conditions. Note that such occupied-to-virtual space mapping through the 1-TDM is not restricted to this type of $|\psi_x\rangle$.

Natural Transition Orbitals

Considering the possibility that several occupied/virtual couples can enter the composition of the electronic transition with comparable relative importance but a different topological message, it is possible to change the basis for the representation of the transition into a diagonal one from which one can clearly identify one (sometimes two) hole and one (sometimes two) electron wave functions, so that in most of the cases only one couple of the so-called Natural Transition Orbitals (NTOs) is required for retrieving all the physics of the transition from the excited state calculation.^{20,28,39-43} In the simplest case (the $|\psi_x\rangle$ defined in equation 14), one can shrink the 1-TDM $z_x^{-1/2}\gamma^{0x}$ into a rectangular \mathbf{T} matrix:

$$(\gamma^{0x})_{rs} = 0 \quad \forall s < N \text{ and/or } r > N \Rightarrow z_x^{-1/2}\gamma^{0x} \equiv \begin{pmatrix} 0_o & \mathbf{T} \\ 0_{v \times o} & 0_v \end{pmatrix} ; \quad (\mathbf{T})_{ic} = z_x^{-1/2}(\gamma^{0x})_{ia}, \quad (17)$$

with $c = a - N$, 0_o and 0_v being the zero matrices with the occupied ($N \times N$) or virtual ($[L - N] \times [L - N]$) space dimensions, and $0_{v \times o}$ being the zero matrix with $(L - N) \times N$ dimensions. This operation can be summarized as

$$z_x^{-1/2}(\gamma^{0x}) \in \mathbb{R}^{L \times L} \quad \longleftrightarrow \quad \mathbf{T} \in \mathbb{R}^{N \times (L - N)}. \quad (18)$$

Following the reduction of the 1-TDM into the rectangular \mathbf{T} , one perform its singular value decomposition⁷¹

$$\exists (\mathbf{O}, \mathbf{V}, \boldsymbol{\lambda}) \mid \mathbf{O}^\dagger \mathbf{T} \mathbf{V} = \boldsymbol{\lambda}. \quad (19)$$

In equation 19, the \mathbf{O} and \mathbf{V} matrices contain in their columns the left and right eigenvectors of \mathbf{T} . Their components are used for the transformation of the SOs into NTOs:

$$\varphi_i^o(\mathbf{r}_1) = \sum_{j=1}^N (\mathbf{O})_{ji} \varphi_j(\mathbf{r}_1) \quad \xleftrightarrow{(\boldsymbol{\lambda})_{ii}} \quad \varphi_i^v(\mathbf{r}_1) = \sum_{j=1}^{L-N} (\mathbf{V})_{ji} \varphi_{N+j}(\mathbf{r}_1), \quad (20)$$

This procedure allows one to condensate the physics of a transition into one couple of one-particle wave functions, with a clear picture of “where the electron comes from and where it goes”.

Natural Difference Orbitals

Similar to the NTOs derivation, when diagonalizing the difference density matrix (see equation 9) instead of the shrunk transition density matrix, it is possible to visualize the so-called Natural Difference Orbitals (NDOs). We can write $\mathbf{m}^r(k)$, the k^{th} component of the r^{th} natural difference orbital (i.e., the eigenvectors of the difference density matrix,^{20,29} stored in the \mathbf{M} matrix – see equation 9) and give the NDOs expression in the real space:

$$\varphi_r^\Delta(\mathbf{r}_1) \xleftrightarrow{\mathbb{R}^3} \mathbf{m}^r(k) = (\mathbf{M})_{kr} \quad , \quad \mathbf{M} \in \mathbb{R}^{L \times L}. \quad (21)$$

Note that since the difference density matrix is the square, Hermitian²⁹ $-\mathbf{T}\mathbf{T}^\dagger \oplus \mathbf{T}^\dagger\mathbf{T}$ matrix, its diagonalization does not produce left (occupied) and right (virtual) eigenvectors, but a set of L eigenvectors. However, according to the definition of $|\psi_x\rangle$ given in equation 14 and given the structure of the corresponding 1-TDM, one can deduce²⁹ that

$$\boldsymbol{\gamma}^d = \mathbf{T}\mathbf{T}^\dagger \oplus 0_v \quad ; \quad \boldsymbol{\gamma}^a = 0_o \oplus \mathbf{T}^\dagger\mathbf{T}, \quad (22)$$

i.e.,

$$\mathbf{M} = \mathbf{O} \oplus \mathbf{V} \quad ; \quad \mathbf{m} = -\boldsymbol{\lambda}\boldsymbol{\lambda}^\dagger \oplus \boldsymbol{\lambda}^\dagger\boldsymbol{\lambda} \quad (23)$$

which means that the occupied and virtual NTOs are the eigenvectors of the detachment and attachment 1-RDM, respectively. Note that in equations 22 and 23, the “ \oplus ” symbol stands for the direct sum of two matrices.

Popular excited states calculation methods such as the Random Phase Approximation (RPA), the Time-Dependent Hartree Fock (TDHF) theory, the Time-Dependent Density Functional Theory (TDDFT) or the GW-Bethe Salpeter equation (BSE) being of particular interest for computing molecular electronic transitions, we did extend the strategies for analyzing the electronic transitions topology to these methods. Refs.^{41,72-77} give more details about these methods. They couple the single excitations (with amplitudes stored in an \mathbf{x} vector) described above (see equation 14) to de-excitations through a \mathbf{y} vector, as expressed for example in the equation of motion linear response (LR) transition operator⁷⁸

$$\hat{\mathcal{T}} = \sum_{i=1}^N \sum_{a=N+1}^L \mathbf{x}_{ia} \hat{a}^\dagger \hat{i} - \mathbf{y}_{ia} \hat{i}^\dagger \hat{a} \quad (24)$$

where \mathbf{x} and \mathbf{y} are the vectors of LR excitation/de-excitation amplitudes. The “ \mathcal{T} ” symbol in this section will refer to mathematical objects derived from RPA/TDHF/TDDFT/BSE methods.

Similar to the singular value decomposition of the shrunk transition density matrix described above, it was proposed for this class of methods to build two rectangular matrices and to produce their left and right eigenvectors. The first one consists in a recast of elementary transition tensors norms stored into a $\boldsymbol{\tau}$ vector into a rectangular $\bar{\mathbf{T}}$ matrix²⁸

$$\sqrt{\mathbf{x}_{ia}^2 + \mathbf{y}_{ia}^2} = \boldsymbol{\tau}_{ia} \Rightarrow \boldsymbol{\tau} \xleftrightarrow{\alpha} \bar{\mathbf{T}} \in \mathbb{R}^{N \times (L-N)} \quad \Rightarrow \quad \exists (\bar{\mathbf{O}}, \bar{\mathbf{V}}, \bar{\boldsymbol{\lambda}}) \mid \bar{\boldsymbol{\lambda}} = \bar{\mathbf{O}}^\dagger \bar{\mathbf{T}} \bar{\mathbf{V}}. \quad (25)$$

Here, the columns of $\bar{\mathbf{O}}$ and $\bar{\mathbf{V}}$ contain the components of occupied $\{\bar{\varphi}^o\}$ and virtual $\{\bar{\varphi}^v\}$ transition orbitals in the canonical spinorbital space.

Another attempt to provide a transposition of the NTOs strategy to the RPA/TDHF/TDDFT/BSE methods consisted in considering as the central quantity of interest the relative weight of an occupied/virtual spinorbital couple.²⁸ From transition operator in equation 24, it appears, due to the non-standard normalization condition corresponding to these methods, i.e.,

$$\sum_{i=1}^N \sum_{a=N+1}^L \mathbf{x}_{ia}^2 - \mathbf{y}_{ia}^2 = 1, \quad (26)$$

that the relative weight of an occupied/virtual canonical couple $(\bar{\boldsymbol{\vartheta}}_{\mathcal{T}})_{ia} = \mathbf{x}_{ia}^2 - \mathbf{y}_{ia}^2$ can lead to the construction of an alternative transition matrix $\mathbf{T}_{\mathcal{T}}$ and to its singular value decomposition, producing the so-called canonical transition orbitals (CTOs)²⁸

$$(\bar{\boldsymbol{\vartheta}}_{\mathcal{T}})_{ia} = \mathbf{x}_{ia}^2 - \mathbf{y}_{ia}^2 \longleftrightarrow \mathbf{T}_{\mathcal{T}} \propto (\boldsymbol{\vartheta}_{\mathcal{T}})_{ia}^{1/2} \longrightarrow (\mathbf{O}_{\mathcal{T}}, \mathbf{V}_{\mathcal{T}}, \boldsymbol{\lambda}_{\mathcal{T}}) \longrightarrow \{\varphi_{\mathcal{T}}^o, \varphi_{\mathcal{T}}^v\} \quad (27)$$

Note that in practise, in most of the cases the squared contributions of the de-excitations (see below) are relatively small when compared to the excitations in the operator in equation 24, so that generally the CTOs and NTOs have very close shapes. For diagnosis purpose, it is possible to assess the relative importance of the hole-particle/particle-hole correlation in such cases²⁸

$$\mu^{0x} = \text{tr}(\mathbf{Y}\mathbf{Y}^\dagger) = \frac{1}{2}(\bar{\boldsymbol{\lambda}} - 1) \quad \bar{\boldsymbol{\lambda}} = \text{tr}(\bar{\boldsymbol{\lambda}}\bar{\boldsymbol{\lambda}}^\dagger). \quad (28)$$

2.3 Quantitative analysis

In addition to providing a clear picture of the transition with visual tools based on charge densities or wave functions, topological analyses of molecular electronic transitions can also be quantitative. Many strategies exist for putting a number on the nature of a transition. Among them, some are based on the segmentation of the geometrical structure of the molecule into molecular fragments, and the evaluation of the inter- or intra-fragment local charge density changes. On the other hand, one can think of systematic (i.e., related to the

system) approaches providing a quantitative assessment of the locality of a charge transfer, or think in terms of amount of displaced charge for example. As we will also see, from some fragment-based approaches one can derive charge transfer numbers which describe the photoinduced electronic structure reorganization or the molecule in its globality. Additionally, some statistical analysis of the exciton size are also possible, as introduced later in this paragraph. Finally, some quantities, indirectly related to the nature of the charge transfer, will be identified.

Prior to the definition of the topological metrics, let's note that for practical reasons the local basis $\{\varphi\}$ is very often expanded into another basis (the basis of atomic functions). This is called the Linear Combination of Atomic Orbitals (LCAO) approximation, and it expresses any spinorbital as

$$\varphi_s(\mathbf{r}_1) = \sum_{\mu=1}^K (\mathbf{C})_{\mu s} \phi_{\mu}(\mathbf{r}_1) \quad 1 \leq s \leq L. \quad (29)$$

In most of the cases, this basis is not orthogonal, and the spatial overlap between two basis functions is computed and stored into the LCAO overlap matrix elements:

$$(\mathbf{S})_{\mu\nu} = \int_{\mathbb{R}^3} d\mathbf{r}_1 \phi_{\mu}^*(\mathbf{r}_1) \phi_{\nu}(\mathbf{r}_1). \quad (30)$$

Since in most of the cases the atomic orbitals are centered on the atomic positions, for a given quantum state $|\psi_m\rangle$, there exist several schemes for trying to evaluate the electronic population of these atomic orbitals, i.e., the amount of charge to be attributed to the different atoms, which gives an approximate mapping of the charge distribution in the molecule:

$$q_A^m = \sum_{\mu \in A} (\mathbf{S}^w \mathbf{C} \gamma_m \mathbf{C}^{\dagger} \mathbf{S}^z)_{\mu\mu} = \sum_{\mu \in A} (\mathbf{S}^w \mathbf{P}_m \mathbf{S}^z)_{\mu\mu} \quad 0 \leq w = 1 - z \leq 1. \quad (31)$$

Note that any combination of w and z follows the constraint that the sum over all the fragments of q_A^m will return the total number of electrons of the system, which makes this type of population analysis quite arbitrary. In these conditions, one can then decide to evaluate the amplitude of the population change for any specific fragment when the molecule goes from its ground to an electronic excited state by computing

$$\Delta q_A^{0x} = q_A^x - q_A^0. \quad (32)$$

Aside from this quantity, one can also try to use the exciton wave function for computing a number relating the nature of an electronic transition: Inserting the LCAO expression of the spinorbitals in the projection of the exciton wave function into the local basis $\{\varphi\}$ gives

$$\begin{aligned} \tilde{\gamma}^{0x}(\mathbf{r}_1; \mathbf{r}'_1) &= \sum_{r,s=1}^L \varphi_r(\mathbf{r}_1) (\gamma^{0x})_{rs} \varphi_s^*(\mathbf{r}'_1) \\ &= \sum_{r,s=1}^L \sum_{\mu,\nu=1}^K (\mathbf{C})_{\mu r} (\gamma^{0x})_{rs} (\mathbf{C}^{\dagger})_{s\nu} \phi_{\mu}(\mathbf{r}_1) \phi_{\nu}^*(\mathbf{r}'_1) \\ &= \sum_{\mu,\nu=1}^K (\mathbf{D}^{0x})_{\mu\nu} \phi_{\mu}(\mathbf{r}_1) \phi_{\nu}^*(\mathbf{r}'_1) \end{aligned}$$

where \mathbf{D}^{0x} is the 1-TDM in the basis of atomic functions. From this expression of $\tilde{\gamma}^{0x}$ and the definition of \mathbf{S} one can evaluate an excitation number as the integral of the product of the exciton wave function with its complex conjugate¹⁹

$$\Omega^{0x} = \int_{\mathbb{R}^3} d\mathbf{r}_1 \int_{\mathbb{R}^3} d\mathbf{r}'_1 \tilde{\gamma}^{0x}(\mathbf{r}_1; \mathbf{r}'_1) \tilde{\gamma}^{0x*}(\mathbf{r}_1; \mathbf{r}'_1) \quad (33)$$

that is, in the LCAO basis:

$$\Omega^{0x} = \int_{\mathbb{R}^3} d\mathbf{r}_1 \int_{\mathbb{R}^3} d\mathbf{r}'_1 \sum_{\mu,\nu=1}^K \sum_{\sigma,\lambda=1}^K (\mathbf{D}^{0x})_{\mu\nu} \phi_\mu(\mathbf{r}_1) \phi_\nu^*(\mathbf{r}'_1) (\mathbf{D}^{0x})_{\mu\nu}^* \phi_\sigma^*(\mathbf{r}_1) \phi_\lambda(\mathbf{r}'_1) \quad (34)$$

and reduces to

$$\Omega^{0x} = \sum_{\mu\nu=1}^K \sum_{\sigma,\lambda=1}^K (\mathbf{D}^{0x})_{\mu\nu} (\mathbf{S})_{\mu\sigma} (\mathbf{D}^{0x\dagger})_{\sigma\lambda} = \text{tr} \left(\mathbf{D}^{0x} \mathbf{S} \mathbf{D}^{0x\dagger} \mathbf{S} \right). \quad (35)$$

This quantity is the number of electrons promoted during the electronic transition process. Obviously, this excitation number is method-dependent, so for example an electronic transition leading to an excited state defined as in equation 14 will return an excitation number of one, because one electron is promoted in total. On the other hand, transitions generated by the operator in equation 24 can lead to promotion numbers superior to one.

Note that if the atomic basis set was orthonormal, the Ω^{0x} quantity would become⁴⁶

$$(\mathbf{S})_{\mu\nu} = \delta_{\mu\nu} \Rightarrow \Omega_{\perp}^{0x} = \sum_{\mu,\nu=1}^K \sum_{\sigma,\lambda=1}^K (\mathbf{D}_{\perp}^{0x})_{\mu\nu} \delta_{\mu\sigma} (\mathbf{D}_{\perp}^{0x\dagger})_{\lambda\sigma} \delta_{\nu\lambda} = \underbrace{\sum_{\mu,\nu=1}^K (\mathbf{D}_{\perp}^{0x})_{\mu\nu} (\mathbf{D}_{\perp}^{0x\dagger})_{\nu\mu}}_{\text{tr}(\mathbf{D}_{\perp}^{0x} \mathbf{D}_{\perp}^{0x\dagger})} = \sum_{\mu,\nu=1}^K |(\mathbf{D}_{\perp}^{0x})_{\mu\nu}|^2 \quad (36)$$

If we are now interested in isolating one $A \rightarrow B$ inter-fragment contribution to the global charge transfer, we can alter the Ω^{0x} by restricting the integration over \mathbf{r}_1 and \mathbf{r}'_1 locally to atoms A and B respectively, which implies that the sum over μ and σ (ν and λ) only holds for indices related to atomic orbitals centered on A (B), and that if we want to keep the expression of a fragment-based Ω^{0x} -like index with matrix products, the matrices entering the definition of Ω^{0x} should be shrunk to cover the atomic spaces span by atoms A and B . To this end, a fragment-based index, Ω_{AB}^{0x} , has been introduced¹⁹

$$\Omega_{AB}^{0x} = \frac{1}{2} \sum_{\mu,\sigma \in A} \sum_{\nu,\lambda \in B} (\mathbf{D}_{AB}^{0x})_{\mu\nu} (\mathbf{S}_B)_{\nu\lambda} (\mathbf{S}_A)_{\mu\sigma} (\mathbf{D}_{AB}^{0x})_{\sigma\lambda} = \frac{1}{2} \sum_{\mu \in A} \sum_{\lambda \in B} (\mathbf{D}_{AB}^{0x} \mathbf{S}_B)_{\mu\lambda} (\mathbf{S}_A \mathbf{D}_{AB}^{0x})_{\mu\lambda} \quad (37)$$

with

$$\mathbf{D}_{AB}^{0x} \in \mathbb{R}^{K_A \times K_B} \quad ; \quad \mathbf{S}_W \in \mathbb{R}^{K_W \times K_W} \quad W = A, B \quad (38)$$

so that one can evaluate a global, normalized charge transfer number,¹⁹ ω_{CT}^{0x} by accounting for every inter-fragment contributions to the total molecular charge transfer (i.e., the cumulated weight of all the singly-excited Slater determinants for which the hole and the particle are located on different fragments):

$$\omega_{\text{CT}}^{0x} = \frac{1}{\Omega^{0x}} \sum_{B \neq A} \sum_A \Omega_{AB}^{0x}. \quad (39)$$

Similar to the relation between Ω^{0x} and Ω_{\perp}^{0x} , one can write an inter-fragment charge transfer number for an orthogonal atomic basis

$$l_{A \rightarrow B}^{0x} = \sum_{\mu \in B} \sum_{\nu \in A} |(\mathbf{D}_{\perp}^{0x})_{\mu\nu}|^2 \quad (40)$$

which was proposed by Luzanov few decades ago.⁴⁶ Note that this $A \rightarrow B$ contribution corresponds schematically to a ψ_{A+B^-} situation, where the charge density is displaced from fragment A to fragment B . Following a similar procedure, one can also compute $l_{B \rightarrow A}$ and $l_{A \rightarrow A} = l_A$ indices corresponding respectively to the ψ_{A-B^+} and to the ψ_{A^*B} (local excitation on A) situations respectively, and derive two quantum metrics,⁴⁶

$$L_A^{0x} = l_A^{0x} + \frac{1}{2} (l_{A \rightarrow B}^{0x} + l_{B \rightarrow A}^{0x}) \quad ; \quad \Delta D_A^{0x} = \sum_{B \neq A} (l_{B \rightarrow A}^{0x} - l_{A \rightarrow B}^{0x}), \quad (41)$$

the first one being an assessment of the so-called total fragment excitation localization (the summed contribution of local excitation and incoming/outcoming charge density fluctuations), while the second one is a measure of the net change of electron density on fragment A , as Luzanov did interpret the two components of ΔD_A^{0x} as “charges of opposite sign flowing between A and B on excitation”. Here, the sign convention we used leads to the interpretation of ΔD_A^{0x} as the quantity related to the charge *gained* by fragment A upon the electronic transition.

In addition to the computation of ω_{CT}^{0x} , it is also possible to evaluate participation ratios¹⁹ in order to count the number of fragments entering a given transition. For this purpose, it is first necessary to evaluate the ratio of fragments entering into the composition of the hole ($\text{PR}_{\text{I}}^{0x}$) and the particle ($\text{PR}_{\text{F}}^{0x}$) before averaging them into PR^{0x}

$$\text{PR}_{\text{I}}^{0x} = \frac{(\Omega^{0x})^2}{\sum_A (\sum_B \Omega_{AB}^{0x})^2} \quad ; \quad \text{PR}_{\text{F}}^{0x} = \frac{(\Omega^{0x})^2}{\sum_B (\sum_A \Omega_{AB}^{0x})^2} \quad ; \quad \text{PR}^{0x} = \frac{1}{2} (\text{PR}_{\text{I}}^{0x} + \text{PR}_{\text{F}}^{0x}) \quad (42)$$

Note that in the definition of $\text{PR}_{\text{I}}^{0x}$ and $\text{PR}_{\text{F}}^{0x}$ it was arbitrarily chosen that fragment A represents the fragment on which all the initial (“I”) orbitals lie, while B is the fragment on which all the final (“F”) orbitals lie. While the PR^{0x} quantity does not inform about the balance of locally excited nature and charge transfer nature for a given excitation, the COH descriptor, expressed as

$$\text{COH} = \frac{1}{\text{PR}} \frac{(\Omega^{0x})^2}{\sum_A \sum_B (\Omega_{AB}^{0x})^2}, \quad (43)$$

has been designed and can provide this information.¹⁹ Note that one can also compute PR^{0x} by combining Ω^{0x} to the 1-TDM singular values¹⁹ contained in $\boldsymbol{\lambda}$:

$$\text{PR}_{\text{NTO}}^{0x} = \frac{(\Omega^{0x})^2}{\sum_i (\boldsymbol{\lambda}_{ii}^4)}. \quad (44)$$

This expression can even be simplified by writing $\text{PR}_{\text{NTO}}^{0x}$ solely as a combination of $\boldsymbol{\lambda}$ elements: If we express Ω^{0x} in the canonical space,

$$\Omega^{0x} = \int_{\mathbb{R}^3} d\mathbf{r}_1 \int_{\mathbb{R}^3} d\mathbf{r}'_1 \sum_{r,s=1}^L \varphi_r(\mathbf{r}_1) (\gamma^{0x})_{rs} \varphi_s^*(\mathbf{r}'_1) \sum_{p,q=1}^L \varphi_p^*(\mathbf{r}_1) (\gamma^{0x})_{pq}^* \varphi_q(\mathbf{r}'_1) \quad (45)$$

which is

$$\Omega^{0x} = \sum_{r,s=1}^L \sum_{p,q=1}^L \underbrace{\int_{\mathbb{R}^3} d\mathbf{r}_1 \varphi_r(\mathbf{r}_1) \varphi_p^*(\mathbf{r}_1)}_{\delta_{rp}} \underbrace{\int_{\mathbb{R}^3} d\mathbf{r}'_1 \varphi_s^*(\mathbf{r}'_1) \varphi_q(\mathbf{r}'_1) (\gamma^{0x})_{rs} (\gamma^{0x})_{pq}^*}_{\delta_{sq}} = \sum_{r,s=1}^L (\gamma^{0x})_{rs} (\gamma^{0x})_{rs}^*. \quad (46)$$

Due to the structure of $\boldsymbol{\gamma}^{0x}$, it becomes

$$\Omega^{0x} = \text{tr}(\boldsymbol{\gamma}^{0x} \boldsymbol{\gamma}^{0x\dagger}) = \text{tr}(\mathbf{T} \mathbf{T}^\dagger). \quad (47)$$

According to equation 19, we can rewrite the \mathbf{T} and its adjoint as the reverse singular value decomposition:

$$\mathbf{T} = \mathbf{O} \boldsymbol{\lambda} \mathbf{V}^\dagger \quad ; \quad \mathbf{T}^\dagger = \mathbf{V} \boldsymbol{\lambda}^\dagger \mathbf{O}^\dagger. \quad (48)$$

Therefore, the product of \mathbf{T} to the right by its adjoint is a square matrix whose eigenvectors are the left eigenvectors entering the singular value decomposition of \mathbf{T}

$$\mathbf{T} \mathbf{T}^\dagger = \mathbf{O} \boldsymbol{\lambda} \mathbf{V}^\dagger \mathbf{V} \boldsymbol{\lambda}^\dagger \mathbf{O}^\dagger \Leftrightarrow \mathbf{O}^\dagger \mathbf{T} \mathbf{T}^\dagger \mathbf{O} = \boldsymbol{\lambda} \boldsymbol{\lambda}^\dagger. \quad (49)$$

Since the trace of a matrix is an unitary invariant, we find that

$$\text{tr}(\mathbf{T}\mathbf{T}^\dagger) = \text{tr}(\boldsymbol{\lambda}\boldsymbol{\lambda}^\dagger) \Rightarrow \Omega^{0x} = \text{tr}(\boldsymbol{\lambda}\boldsymbol{\lambda}^\dagger) \quad (50)$$

so that $\text{PR}_{\text{NTO}}^{0x}$ becomes

$$\text{PR}_{\text{NTO}}^{0x} = \frac{(\sum_i (\boldsymbol{\lambda}\boldsymbol{\lambda}^\dagger)_{ii})^2}{\sum_i (\boldsymbol{\lambda}\boldsymbol{\lambda}^\dagger)_{ii}^2} \quad (51)$$

which is equal to Luzanov's collectivity measure metric,⁴⁵ κ^{CIS} .

Another interesting characterization of the electronic transition is given by the computation of global charge transfer numbers related to the nature of the transition.⁵⁴ Starting from the state densities, one can for example assess the amount of charge transferred during a transition

$$q_{\text{CT}} = \frac{1}{2} \sum_{s=+,-} \int_{\mathbb{R}^3} d\mathbf{r} n_s(\mathbf{r}) \quad (52)$$

which should not be confused with the amount of charge displaced during the transition. This distinction is related to the difference between the hole and particle (i.e., detachment/attachment) densities and the difference densities mentioned above.⁵⁸

In addition to q_{CT} , one can also compute the distance between the centroid of n_- and n_+ . For this purpose, we define a position vector⁵⁴ $\boldsymbol{\xi} = (\xi_1, \xi_2, \xi_3) = (x, y, z)$ and we evaluate its expectation value by integrating the product of its components with n_- and n_+

$$\xi_{i,s}^{0x} = q_{\text{CT}}^{-1} \int_{\mathbb{R}^3} d\mathbf{r}_1 n_s(\mathbf{r}_1) \xi_i \quad i = 1, 2, 3 \quad ; \quad s = \pm. \quad (53)$$

The three components of the two centroid position vectors are then compiled into the \mathbf{R}_\pm vectors, and the norm of the difference between these two vectors represents the distance between the two centroids in the Euclidean space:⁵⁴

$$\mathbf{R}_\pm = (\xi_{1,\pm}^{0x}, \xi_{2,\pm}^{0x}, \xi_{3,\pm}^{0x}) \Rightarrow D_{\text{CT}} = |\mathbf{R}_+ - \mathbf{R}_-| = \left\{ \sum_{i=1}^3 (\xi_{i,+}^{0x} - \xi_{i,-}^{0x})^2 \right\}^{1/2} \quad (54)$$

Note also that the product of the charge transferred by the charge transfer distance gives the norm of a ‘‘charge transfer dipole moment’’:⁵⁴

$$|\boldsymbol{\mu}_{\text{CT}}| = q_{\text{CT}} D_{\text{CT}}. \quad (55)$$

Besides the charge transfer numbers derived from state densities, one can also use the detachment/attachment densities for quantitatively probing the nature of an electronic transition. For instance, the locality of the charge displacement can be evaluated through the computation of the hole/particle spatial overlap⁵⁷

$$\phi_S = \vartheta_x^{-1} \int_{\mathbb{R}^3} d\mathbf{r} \sqrt{n_d(\mathbf{r})n_a(\mathbf{r})} \in [0;1] \quad ; \quad \vartheta_x = \frac{1}{2} \sum_{q=d,a} \int_{\mathbb{R}^3} d\mathbf{r} n_q(\mathbf{r}) \quad (56)$$

This quantity, combined with the normalized charge transferred⁶⁰

$$\frac{\vartheta_x^{-1}}{2} \sum_{s=+,-} \int_{\mathbb{R}^3} d\mathbf{r} n_s(\mathbf{r}) = \tilde{\varphi} \in [0;1] \quad (57)$$

gives a global quantum metric jointly relating the locality of the exciton and the amount of charge transferred during the transition⁶⁰

$$\psi = 2\pi^{-1} \underbrace{\arctan\left(\frac{\phi_S}{\tilde{\varphi}}\right)}_{\theta_S} = \frac{2\theta_S}{\pi} \in [0;1]. \quad (58)$$

where θ_S is the angle between the real axis of a complex plane and the projection of ϕ_S and $\tilde{\varphi}$ in that plane (see Ref.⁶⁰ for more details). Note that, as in the derivation of the intercentroid distance between the net depleted/accumulated charge densities (see equations 53 and 54), one can also compute the distance between the centroid of detachment and attachment densities. This quantity, written ζ in Ref.,⁵⁸ deviates from D_{CT} when the overlap between the hole and the particle increases (see figure 2 from Ref.⁵⁸).

It is worth pointing out that, since the difference between the attachment and detachment density matrices returns the difference density matrix, and due to the unequivocality of the density matrix-to-charge density mapping, any function or quantity involving n_+ or n_- (the q_{CT} and D_{CT} numbers for example) could be equivalently derived from state densities or from detachment/attachment 1-CD.⁵⁸ However, it has been demonstrated that the integral of the detachment (or attachment) 1-CD is an upper bound to the one of n_{\pm} , which justifies its use as a normalization term for $\tilde{\varphi}$ (where the “ \sim ” symbol above φ in $\tilde{\varphi}$ was used to notify that the n_{\pm} functions used for computing it were derived from detachment/attachment density difference, though this detail was dispensable).^{58,60}

Note also that in parallel to the hole/particle spatial overlap (ϕ_S), one can also compute the hole/particle entanglement entropy²⁶ $S_{H|E}$ which is directly related to the effective number of entangled states²⁶ Z_{HE}

$$S_{H|E} = - \sum_i (\boldsymbol{\lambda}\boldsymbol{\lambda}^\dagger)_{ii} \log_2 (\boldsymbol{\lambda}\boldsymbol{\lambda}^\dagger)_{ii} \quad ; \quad Z_{HE} = \left(\prod_i (\boldsymbol{\lambda}\boldsymbol{\lambda}^\dagger)_{ii}^{(\boldsymbol{\lambda}\boldsymbol{\lambda}^\dagger)_{ii}} \right)^{-1} = 2^{S_{H|E}} \quad (59)$$

Besides the derivation of charge transfer numbers from the manipulation and integration of 1-CD functions, one can also use one-particle wave functions to gain quantitative insights into the nature of electronic transitions. For example, a Λ descriptor was designed by Tozer and co-workers in order to perform a diagnostic test of exchange-correlation functionals for TDDFT calculations. This descriptor writes⁵³

$$\Lambda = \frac{\sum_{i=1}^N \sum_{a=N+1}^L \kappa_{ia}^2 O_{ia}}{\sum_{i=1}^N \sum_{a=N+1}^L \kappa_{ia}^2} \quad \kappa_{ia} = \mathbf{x}_{ia} + \mathbf{y}_{ia} \quad ; \quad O_{ia} = \int_{\mathbb{R}^3} d\mathbf{r}_1 |\varphi_i(\mathbf{r}_1)| |\varphi_a(\mathbf{r}_1)| \quad (60)$$

and was related to the error observed on the transition energies of molecules, when computed with different types of exchange-correlation functionals. The κ elements were also used for constructing another charge transfer metric, Δr

$$\Delta r = \frac{\sum_{i=1}^N \sum_{a=N+1}^L \kappa_{ia}^2 |\langle \varphi_a | \mathbf{r}_1 | \varphi_a \rangle - \langle \varphi_i | \mathbf{r}_1 | \varphi_i \rangle|}{\sum_{i=1}^N \sum_{a=N+1}^L \kappa_{ia}^2} \quad (61)$$

related to the spatial structure of the exciton (more particularly, the space covered during the excitation).⁵⁶ As when we wrote PR^{0x} using the singular values of the 1-TDM, the Δr metric was also transposed to the NTO basis where κ is replaced by $\boldsymbol{\lambda}\boldsymbol{\lambda}^\dagger$, and the occupied and virtual canonical orbitals were replaced by the occupied and virtual NTOs for constructing the Δr_{NTO} index.⁵⁹

Independently from the development of Δr , D_{CT} and ζ , two descriptors were also designed²⁴ for relating the root-mean-square deviation separation between the hole and the particle (d_{exc}) and relative electron/hole separation distance ($d_{h \rightarrow e}$):

$$d_{exc} = \sqrt{\langle |\mathbf{r}_1 - \mathbf{r}'_1|^2 \rangle} \quad ; \quad d_{h \rightarrow e} = |\langle \mathbf{r}'_1 - \mathbf{r}_1 \rangle| \quad (62)$$

with $d_{h \rightarrow e} \leq d_{exc}$. Note that when evaluating these two expectation values, the normalized integration is performed over the hole and the particle coordinates. Such integral for any operator \hat{O} gives²²

$$\langle \hat{O} \rangle = \frac{1}{\Omega^{0x}} \int_{\mathbb{R}^3} d\mathbf{r}_1 \int_{\mathbb{R}^3} d\mathbf{r}'_1 \tilde{\gamma}^{0x}(\mathbf{r}_1, \mathbf{r}'_1) \hat{O} \tilde{\gamma}^{0x*}(\mathbf{r}_1, \mathbf{r}'_1). \quad (63)$$

Furthermore, it is also possible to estimate the covariance between the hole and the particle position vectors²⁴

$$\text{COV}(\mathbf{r}_1, \mathbf{r}'_1) = \langle \mathbf{r}_1 \cdot \mathbf{r}'_1 \rangle - \langle \mathbf{r}_1 \rangle \cdot \langle \mathbf{r}'_1 \rangle \quad (64)$$

as well as the Pearson correlation coefficient applied to the hole/particle statistical spatial distribution²⁴

$$R_{eh} = \sigma_{\mathbf{r}_1}^{-1} \sigma_{\mathbf{r}'_1}^{-1} \text{COV}(\mathbf{r}_1, \mathbf{r}'_1) \quad (65)$$

which is the covariance normalized with the standard deviations of the hole/particle positions²⁴

$$\sigma_{\mathbf{r}_j} = \sqrt{\langle \mathbf{r}_j^2 \rangle - \langle \mathbf{r}_j \rangle^2} \quad \mathbf{r}_j = \mathbf{r}_1, \mathbf{r}'_1. \quad (66)$$

The σ function is also employed for completing the above mentioned Δr with a statistical descriptor, $\Delta\sigma$, defined as⁵⁹

$$\Delta\sigma = \frac{\sum_{i=1}^N \sum_{a=N+1}^L \kappa_{ia}^2 |\sigma_a - \sigma_i|}{\sum_{i=1}^N \sum_{a=N+1}^L \kappa_{ia}^2} \quad ; \quad \sigma_p = \sqrt{\langle \varphi_p | \mathbf{r}_1^2 | \varphi_p \rangle - \langle \varphi_p | \mathbf{r}_1 | \varphi_p \rangle^2} \quad (67)$$

which is then simply added to Δr in order to give⁵⁹

$$\Gamma = \Delta r + \Delta\sigma. \quad (68)$$

Note finally that this metric can also be derived using the natural transition orbitals rather than the canonical orbitals.⁵⁹

3 Electronic structure and charge generation properties of dye-sensitized metal oxides

3.1 Dye adsorption and energy levels line-up: electrostatic and charge transfer

The primary dye/semiconductor interactions are mediated by the dye adsorption mode onto the semiconductor surface, which directly influences the interfacial electrostatic and the electronic coupling between the molecule and the substrate, yielding sizeable changes in their relative energy level alignment. A crucial characteristic for efficient dyes is the presence of suitable functional groups able to strongly bind to the semiconducting oxide surface. To favor ultrafast electron injection, the anchoring group indeed should coincide, or be very close (conjugated), to the dye acceptor unit, where the photo-excited electrons are spatially confined. This promotes electronic coupling between the donor levels of the excited dye and the delocalized acceptor levels of the semiconductor conduction band, and helps the charge injection process.^{79–81} The sensitizer's anchoring group should also provide stable grafting of the dye onto semiconductor surface, thus leading to long-term device stability.

The anchoring mechanism of the largely employed carboxylic acid group to the TiO₂ surface can be exemplified referring to the coordination modes of the carboxylate fragment (COO⁻) to metal ions; there are basically three typical coordination schemes: monodentate, bidentate chelating and bidentate bridging, with the last one usually disregarded since it is less stable. Along with experimental investigations, a number of theoretical studies on the dye adsorption modes on the TiO₂ surface have been published,^{82–91} starting from the pivotal work by Vittadini et al. on the formic acid adsorption on the TiO₂ anatase (101) surface.⁸⁹ In some cases, calculations showed that for organic dyes bearing a carboxylic acid as anchoring group, the preferred adsorption mode was bidentate bridging, with one proton transferred to a nearby surface oxygen, while the monodentate anchoring is usually predicted to be less stable, although some dependency of the relative stability of these two anchoring modes on the employed computational methodology has been outlined.^{89,92}

The energetics of the TiO₂ conduction band are known to depend on several factors, such as the local pH,^{93–95} the concentration of potential determining ions (*e.g.* Li⁺)^{95,96} and, possibly in relation to acid-base equilibria, also on the nature of the electrolyte solvent.^{96,97} The role of surface adsorbed molecules, including the dye, in determining the TiO₂ CB energetics is much less clear.^{84,98–105} Different works on ruthenium dyes have shown a correlation between the dye protonation state and the DSC performance,^{84,102,105} with dyes carrying a higher number of protons leading to higher photocurrent values, J_{sc} , but lower open circuit voltage, V_{oc} . An interesting correlation between the dipole moment of co-adsorbing species, mainly substituted benzoic acids, and the corresponding DSC V_{oc} was observed by Rühle *et al.*,¹⁰¹ who pointed out a linear relationship between the dye coverage (N), the dipole (μ) component normal to the surface (θ is the molecule tilting angle) and the potential shift (ΔV) at the interface affecting the TiO₂ CB energy:

$$\Delta V = \frac{N\mu \cos \theta}{\varepsilon \varepsilon_0} \quad (69)$$

where ε is the dielectric constant of the dye monolayer and ε_0 is the dielectric permittivity of vacuum. For ruthenium dyes, a correlation between the dye adsorption mode and the corresponding DSC V_{oc} has been observed.⁸⁴ Later works on solid-state DSC has clearly shown a greater than 100 mV TiO₂ conduction band shift between a heteroleptic ruthenium dye and an organic dye, which was interpreted in terms of a dipole-induced TiO₂ CB shift of different sign.¹⁰⁶ Such shifts are generally more difficult to be observed in DSC based on a liquid electrolyte,¹⁰⁷ in which the high ion strength and the effect of thermal motion may hinder the role of interface dipoles. Nevertheless, Kusama *et al.* reported a combined experimental and theoretical study which showed a clear correlation between the dipole moment of electrolyte additives and their DSC V_{oc} .¹⁰⁴

As a matter of fact, when a dye binds to a semiconductor surface, two effects might be at work: (a) the aforementioned electrostatic (EL) effect, due to the dye dipole moment; and (b) the effect of the charge transfer (CT) between the dye and the semiconductor, which may accompany the dye-semiconductor bond formation. We have used the so-termed Charge Displacement (CD) analysis,¹⁰⁸ to investigate the adsorption of several prototypical organic dyes and co-adsorbents on TiO₂ models, quantifying and rationalizing the effects of EL and CT contributions to the TiO₂ CB energetics.⁶²

Similar to the ESCD strategy (see equation 8), one can analyze the electron density rearrangement by defining the charge displacement (CD) along the z direction as:

$$\Delta q(z) = \int_{-\infty}^z dz' \int_{-\infty}^{+\infty} \int_{-\infty}^{+\infty} \Delta \rho(x, y, z') dx dy. \quad (70)$$

where $\Delta \rho$ is the electron density difference and Δq measures, at each point along the z axis, the electron charge that, upon formation of the adduct, is transferred from the right to the left side of the perpendicular plane through z (a negative value thus corresponds to electron flow from left to right).

In this case, after defining the average TiO₂ surface plane, we choose as integration direction (z) that perpendicular to this plane and passing through the carboxylic carbon on the anchoring group of the dye. The dye-TiO₂ geometry was fully relaxed in *vacuo* using the PBE exchange correlation functional with the ADF program package;¹⁰⁹ a TZVP(DZVP) basis set for Ti (H, C, N, O, S) atoms was adopted. The electron density was obtained by a DFT/B3LYP single point calculation employing the SVP basis set and the solvent (acetonitrile) have been described by means of the C-PCM solvation model¹¹⁰ as implemented in Gaussian 09 (G09).¹¹¹ In Figure 1 we show the isodensity contour plot of the electron density difference and the CD curve, calculated by equation 70 for the prototypical L0 dye adsorbed onto a (TiO₂)₃₈ cluster in the bidentate bridging (BB) configuration. We can see significant charge depletion lobes in the areas around the carboxylic group, the nitrogen atom of the nitrile group and the phenyl bound to the cyanoacrylic moiety. Charge accumulation lobes can be seen instead on the central carbon of the cyanoacrylic anchoring group of the sensitizer, in proximity of the proton detached from the dye and adsorbed on the TiO₂ surface and, in particular, in regions of the semiconductor cluster. Note that the curve is largely positive across the entire adduct, implying a continuous charge transfer from the dye to the TiO₂. The maximum of the CD curve in the inter-fragment region is 0.36 electrons. Different dyes adsorbed in the same bidentate adsorption mode showed little variations in the amount of CT, while the molecular monodentate adsorption geometry yielded to a much smaller CT.

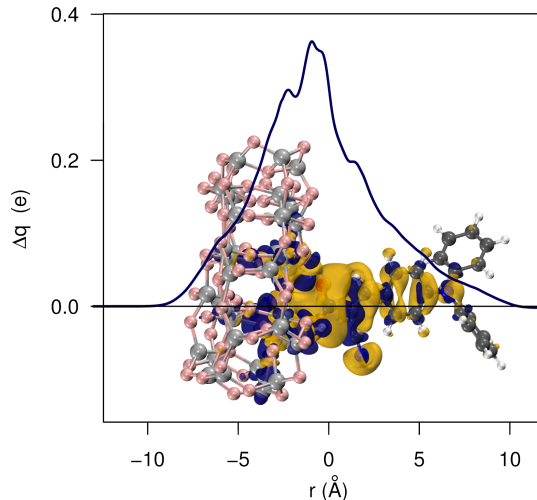


figure 1: Isodensity contour plot and charge displacement curve for L0 adsorbed onto TiO_2 in a BB configuration. Yellow surfaces identify regions in which the electron density decreases whereas zones of density accumulation are marked by dark blue surfaces. The density value at the surfaces is $\pm 0.0005 \text{ e au}^{-3}$. Reprinted from Ref. ⁶² by permission of The Royal Society of Chemistry.

Assuming that this marked charge redistribution, along with a pure electrostatic (EL) contribution due to the dye dipole, induce significant modifications on the TiO_2 CB edge, one can formulate a simple interpretative model by expressing the total shift, ΔCB_{TOT} , as the sum of the two main effects strictly related to the dye sensitizer ($\Delta CB_{TOT} = \Delta CB_{EL} + \Delta CB_{CT}$).

Concerning the EL effect, we evaluated the CB shift in relation to the electrostatic potential generated by the dye molecule rather than with its standalone dipole moment. This quantity represents the effective average electrostatic potential generated by the dye charge distribution in the region of the first semiconductor titanium layer. We demonstrated that the electrostatic potential generated by the dye charge distribution correlates linearly and very accurately with the observed TiO_2 conduction band shift. This implies that a direct correlation between the dye dipole and the observed conduction band shift effectively exists only for dyes of similar structure and dimensions. The estimated electrostatic contribution to the conduction band shift amounts to about 40% of the total calculated shifts. Considering the pronounced ground state dye/semiconductor charge transfer, we investigated the supposition that the remaining contribution to the semiconductor CB shift is directly due to charge transfer effects. We established that there is indeed near-exact proportionality between the amount of charge transfer calculated by the charge displacement analysis and the residual contribution to the conduction band shift. We thus found that the CT induced CB shift may be as large as 60% of the total shift.

While hybridization of the dye/semiconductor molecular orbitals translates into a considerable net charge transfer from the dye to the TiO_2 CB, the electrostatic effect dominates in the case of decoupled subsystems, as we shall discuss below for the coumarin C343-sensitized nickel oxide surface.⁶³ Contrary to the rich literature on the functionalization of TiO_2 substrates by molecular sensitizers,^{88, 112–114, 114–119} the characterization of the electronic and structural properties of dye-sensitized NiO interfaces in both *p*-type DSCs and water reduction photocathodes is still modest. In the few theoretical work reported so far,^{63, 120–122} the energy level alignment across the interface, and in particular the relative position of the dye's HOMO with respect to NiO's VB, ruling the hole injection driving force, was found to be extremely sensitive to the anchoring group and binding mode (monodentate, bidentate, tridentate) of the dye. We have recently characterized the interaction of a derivative the coumarin C343 dye, featuring a terminal phosphonic acid ($-\text{PO}(\text{OH})_2$) anchoring group and the (100) NiO surface. We have considered two possible conformers:^{123, 124} one where one of the H atoms of the phosphonate is H-bonded to the oxygen of the carbonyl group of the coumarin (H-up), the other where both H atoms of

the phosphonate point away from it (H-down) (see Figure 2). The DFT calculations (Quantum ESPRESSO software¹²⁵) were carried out using the PBE exchange and correlation functional, with a Hubbard U term of 4.6 eV.¹²⁶ We used ultrasoft pseudopotentials¹²⁷ and a plane waves basis set, with a cutoff of 30 Ry for the wave functions and 300 Ry for the charge density. Dispersion corrections to DFT were modeled using Grimme’s method.¹²⁸ Further details can be found in the original paper.⁶³ In gas phase, the H-bonded isomer is slightly favored, by 0.20 eV using the PBE functional.

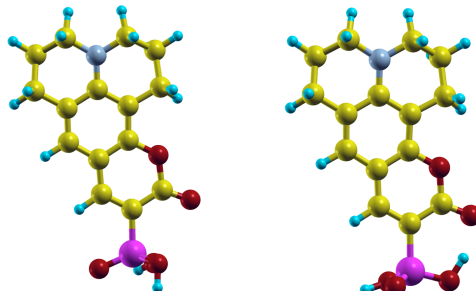


figure 2: Optimized geometries of two isomers of the C343 dye molecule with a phosphonic acid anchoring group. Left: H-down. Right: H-up.

In line with previous work¹²⁰ the bidentate binding was found to be the most stable anchoring mode of the $\text{CH}_3\text{-PO}(\text{OH})_2$ group onto the NiO(100) surface with an adsorption energy for the H-up and H-down C343 isomers adsorbed on a 6-layer surface slab of -1.30 eV and -1.06 eV, respectively. In addition to the different adsorption energy, favoring the H-up configuration, the PDOS for the two systems in 3 show that there is also a large influence on the position of the molecular orbitals of the dye with respect to the NiO levels. In particular the HOMO of the dye lies 1.1 eV below the valence band maximum (VBM) in the H-up configuration, while it is 0.1 eV above the VBM in the H-down geometry, the latter coinciding with the relative alignment predicted for the isolated components. The explanation for this lies in the fact that the different adsorption geometries result in different interfacial dipoles, which shift the electrostatic potential in the region of the dye relative to the potential of the NiO slab (the shift in the electrostatic potential perpendicular to the slab is exactly 1.2 eV in the region of the dye).⁶³ Being essentially decoupled from the NiO slab (see plot of the corresponding Kohn-Sham state in Figure 3 and the sharp peak of the dye’s HOMO), the HOMO of the dye experiences a rigid shift in energy with respect to the valence band of NiO as the positively charged H atom of the anchoring group moves from the H-down to the H-up configuration.

3.2 Charge separation and electron injection rates

The first and most important electron-transfer process occurring at the dye/semiconductor interface is the charge injection from the photoexcited dye to the CB of the substrate.¹²⁹ The injection quantum yield η_{inj} (photons absorbed by the dye that end up in electron injected into the CB of the metal oxide) is given by:

$$\eta_{inj} = \frac{k_{inj}}{k_{inj} + k_0 + k_q} \quad (71)$$

where k_0 is the rate constant for radiative and nonradiative decay of the excited state of stand-alone sensitizer and k_q represents all possible deactivation channels of the dye’s excited state in the cell different from electron injection. The remarkable fortune obtained by ruthenium dyes in the DSC field is at least partially ascribable to their high electron injection quantum yields,^{99,130–134} originating from the large values of the electron injection rates (~ 100 ps) but also from the long lifetimes (from tens to hundreds of nanoseconds) of the lowest-energy triplet state (mostly responsible of the electron injection) that strongly reduce the term k_0 in equation 71.¹³⁴ In Ru(II) compounds, electron injection is also assisted by the small recombination rate constants as a consequence of an efficient electron-hole separation and by their peculiar grafting geometry, which adequately hinders the

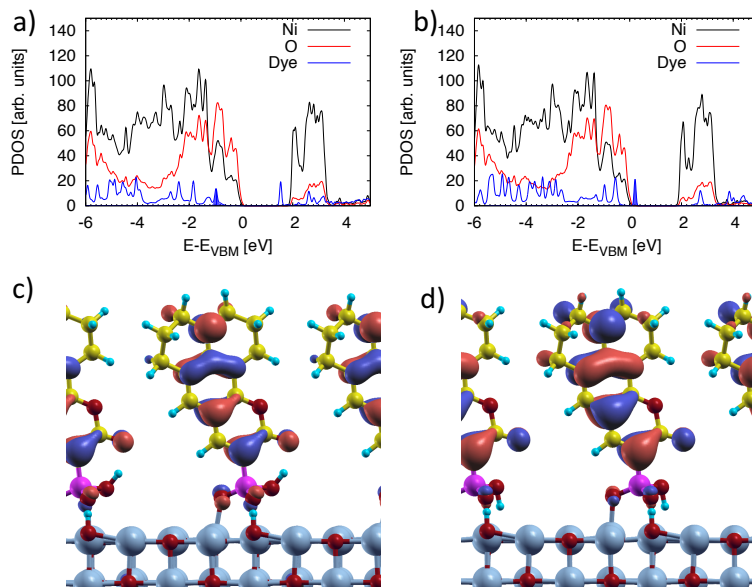


figure 3: The C343/NiO(100) system in vacuum in the bidentate anchoring geometry, evaluated using the PBE+U approach. We show the PDOS of: (a) the H-up geometry; (b) H-down geometry. The blue shaded areas represent the projections on the HOMO of the isolated dye. The isosurfaces of the dye's HOMO Kohn-Sham state are shown in panel (c) for the H-up geometry and panel (d) the H-down geometry. In both cases the dye's HOMO is fully localized on the dye, with no significant weight on the NiO slab. Reprinted with permission from (Piccinin, S.; Rocca, D; Pastore, M. Role of Solvent in the Energy Level Alignment of Dye-Sensitized NiO Interfaces *J. Phys. Chem. C*, **2017**, *121*, 22286-22294). Copyright (2017) American Chemical Society.

interfacial aggregation phenomena.¹³⁴ However, despite its record efficiencies, in the view of large-scale solar energy production, ruthenium suffers from serious drawbacks, which potentially limit its widespread applicability, mainly related to its toxicity and scarcity. This has motivated continuous research efforts to develop valuable alternatives, exploiting earth-abundant, less expensive and environmentally friendly d-block metal (for example iron and copper) complexes.^{135–139} Despite an intense absorption by the metal-to-ligand charge transfer (MLCT) states, however, conventional Fe(II)-polypyridyl complexes are, unfortunately, characterized by an ultrafast (ca. 100 fs) deactivation to low-lying Metal Centered (MC) states, proceeding via the triplet ^3MC and ultimately populating the quintuplet $^5\text{T}_2$ state,^{140–142} which impedes electron injection into the sensitized semiconductor.¹⁴³ Recent breakthroughs have been obtained by the development of Fe(II) complexes with strongly electron σ -donating N-heterocyclic carbene (NHC) ligands,^{38,144–148} reaching record lifetimes of hundreds of picoseconds.^{149,150} On the other hand, for organic dyes the thermalization to the triplet state is much slower than the injection and emission processes, and hence the system transfers the photo-excited electron directly from the lowest singlet state. Even though the injection process from the singlet is faster compared to that from the triplet state, the singlet lifetime can be about 20-fold shorter, opening the way to a considerably larger competition between the injection process and the radiative decay, yielding to lower quantum yields.¹³⁴ Moreover, organic chromophores are usually characterized by faster recombination of the injected electron with the oxidized dye when compared to metal complexes, possibly originated by a generally closer localization of the dye highest occupied molecular orbital (HOMO) to the TiO_2 surface,¹³⁴ also boosted by particular grafting configurations.

The theoretical description of excited-state electron injection into wide-bandgap semiconductors was first proposed by Marcus and Gerischer.^{151–153} Under the weak coupling regime, the rate constant (k_{inj}) for the electron transfer from a single dye's d state to the many acceptor states k of the metal oxide can be obtained

using the Fermi Golden Rule as:

$$k_{inj} = \frac{2\pi}{\hbar} \sum_k |V_{dk}|^2 \rho(\varepsilon_k) \quad (72)$$

where $\rho(\varepsilon_k)$ is the density of semiconductor acceptor states (DOS) at the energy ε_k , V_{dk} the electronic coupling between the (diabatic) donor d state and the k th acceptor state in TiO_2 , and \hbar Planck's constant. A rapid estimate of the electron injection times can be attained by resorting to the Newns-Anderson model.^{154–159} This approach provides a fast assessment of the effects of the adsorption on the molecule electronic levels (generally only the dye LUMO is analyzed), characterizing them in terms of an energy shift relative to the free system and a lifetime broadening, $\hbar\Gamma$, defined by a Lorentzian distribution resulting from the decay of the dye excited state, approximated by the dye LUMO, coupled to the continuum of the TiO_2 CB states^{64, 80–82, 160, 161} To obtain these quantities one has to calculate the projected density of states (PDOS) relative to the dye's LUMO in the dye- TiO_2 complex. When the system's molecular orbitals in a certain atomic basis are expanded, the contributions p_i to the dye's LUMO PDOS are defined by the relation:

$$p_i = \frac{\sum_j^{A \in \text{dye}} (c_{ij}^A)^2}{\sum_j^n (c_{ij}^A)^2} \quad (73)$$

where c_{ij}^A are the expansion coefficients of the molecular orbitals of the complex on the basis function of atom A belonging to the dye.

The center of this distribution gives the energy of the dye's LUMO grafted on TiO_2 , $E_{LUMO}(ads)$, and it can be obtained as:

$$E_{LUMO}(ads) = \sum_i p_i \varepsilon_i. \quad (74)$$

On the other hand, the width of the LUMO broadening can be estimated as a mean deviation of a distribution centered at the $E_{LUMO}(ads)$ energy value through the equation:

$$\hbar\Gamma = \sum_i p_i |\varepsilon_i - E_{LUMO}(ads)|. \quad (75)$$

The Newns-Anderson model, despite its simplicity and effectiveness, does not allow the direct calculation of the coupling between the dye and semiconductor states, leading directly to the injection time. To do that, one can use the model proposed by Thoss and co-workers.^{162, 163} This approach, based on the localization of the molecular orbitals of the complex on the donor (d) and acceptor (a) species, gives the diabatic semiconductor DOS and the diabatic dye's LUMO, as well as the explicit coupling between the dye's LUMO and the manifold of the semiconductor acceptors states. The product between the square of the electronic coupling elements, $|V_{dk}|^2$, and the TiO_2 density of states, $\rho(\varepsilon_k)$, defines the electron transfer probability distribution, $\Gamma(\varepsilon_k)$. Finally, electron transfer times can be evaluated by $\tau(\text{fs}) = 658/\Gamma(\text{meV})$.

In the following we will review the application of the two above mentioned approaches to TiO_2 substrates (bares and protonates) sensitized by organic dyes having different electronic structure and excited states properties.⁶⁴

3.2.1 Role of the Dye Molecular Structure and of the CB Position on Injection Rates

Two popular cyanoacrylic based conjugated dyes (Figure 4) differing for the extension of the π bridge, namely, L0,^{103, 164, 165} and JK2^{15, 106, 166, 167} will be examined.⁶⁴ For the latter we also considered a different configuration, obtained by twisting of 90° the C-C bond linking the cyanoacrylic anchoring and thiophene units (JK2-T, see below), to assess the effects of breaking of the electron conjugation. Then, to enrich our set, also an indoline-based dye, D102, was included.¹⁶⁶ As shown in Figure 4, the sensitizers have been adsorbed onto the TiO_2 surface by the carboxylic group in the BB configuration, upon deprotonation and H transfer to the surface.^{103, 168}

The TiO_2 surface has been modeled by a $(\text{TiO}_2)_{82}$ cluster,¹⁶⁹ obtained by an appropriate "cut" of an anatase slab exposing the majority (101) surface.¹⁷⁰ To model surface protonation we adsorbed on the TiO_2 cluster

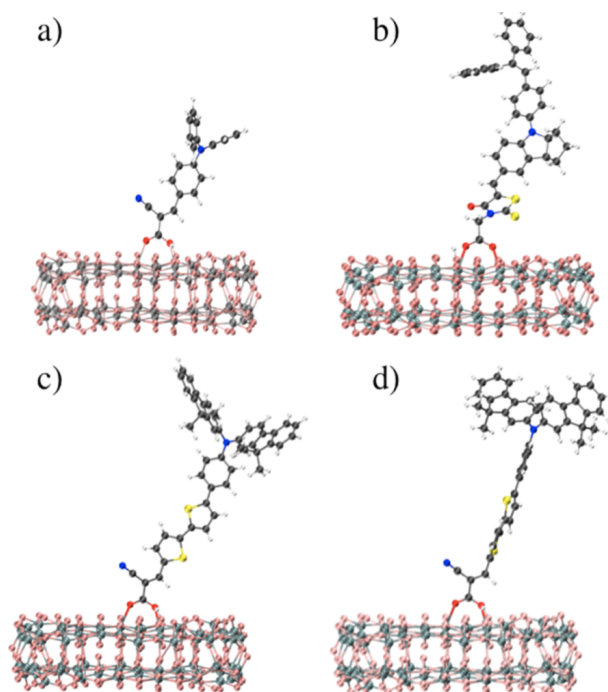


figure 4: Optimized geometries of the L0 (a), D102 (b), JK2 (c), and JK2-T (d) dyes adsorbed onto the $(\text{TiO}_2)_{82}$ cluster in bridged bidentate (BB) anchoring geometry. Reprinted with permission from (Ronca, E.; Marotta, G.; Pastore, M; De Angelis, F. Effect of Sensitizer Structure and TiO_2 Protonation on Charge Generation in Dye-Sensitized Solar Cells *J. Phys. Chem. C*, **2014**, *118*, 16927-16940). Copyright (2014) American Chemical Society.

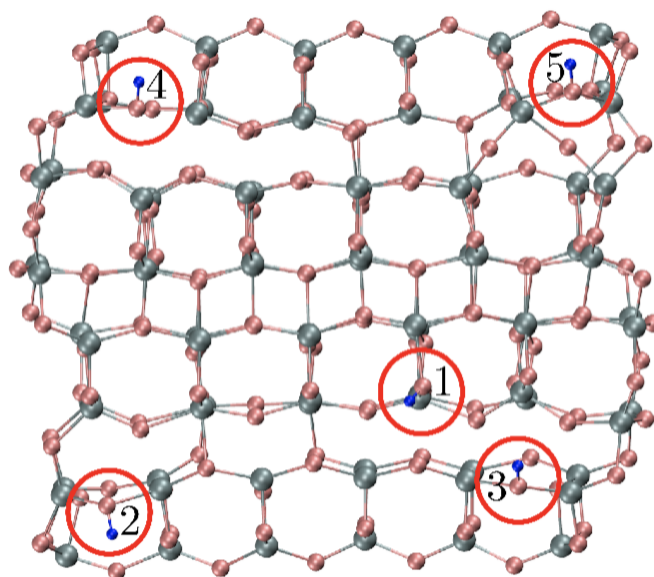


figure 5: Scheme of the adsorption position of protons on the $(\text{TiO}_2)_{82}$ cluster. Reprinted with permission from (Ronca, E.; Marotta, G.; Pastore, M; De Angelis, F. Effect of Sensitizer Structure and TiO_2 Protonation on Charge Generation in Dye-Sensitized Solar Cells *J. Phys. Chem. C*, **2014**, *118*, 16927-16940). Copyright (2014) American Chemical Society.

surface an increasing number of protons, as shown in Figure 5. The first proton was placed at the center of the cluster, close to the dye, while the other four H^+ 's have been progressively adsorbed at the cluster corners.

The dye@(TiO₂)₈₂ equilibrium geometries were obtained in *vacuo* with the ADF program package¹⁰⁹ employing the PBE exchange correlation functional with the TZP (DZP) basis set for Ti (H,C,N,O,S) atoms. The Projected Density of States (PDOS) relative to the dye's LUMO were obtained by single-point calculations performed at the DFT/B3LYP level of theory using the SVP basis set on the ADF-optimized geometries. Solvation effects (acetonitrile) were modeled by means of the C-PCM¹¹⁰ method implemented in the Gaussian 09 (G09) suite.¹¹¹

The results for the investigated systems in the neutral monoprotonated form (hereafter termed 1H), starting with the Newns-Anderson analysis of the dye- TiO₂ complexes, are reported in Figure 6, where we also report the corresponding Lorentzian distribution and the PDOS relative to the semiconductor in the presence of the dye.

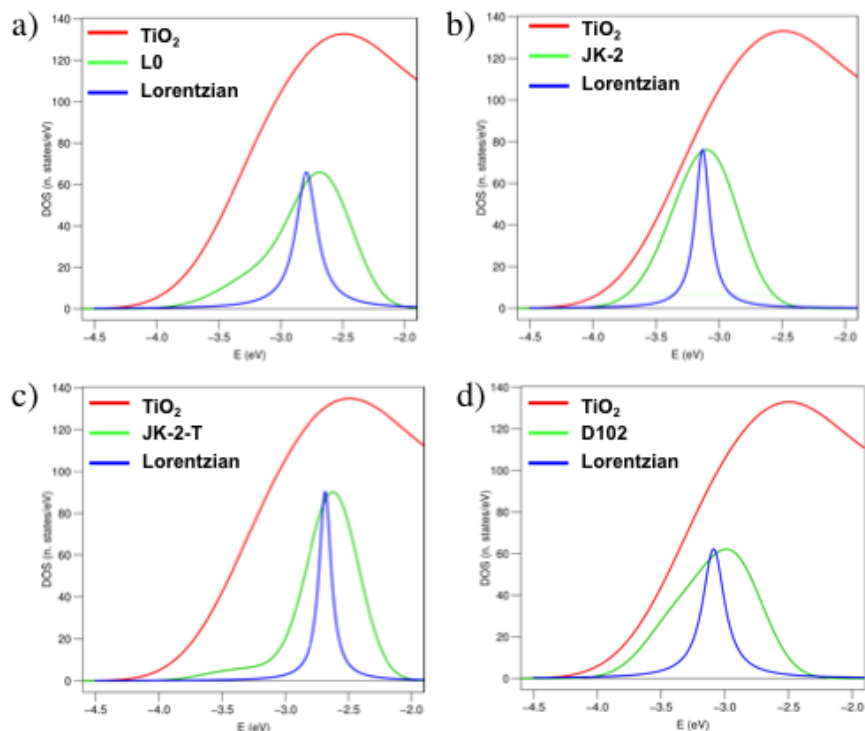


figure 6: PDOS relative to the sensitizer and to TiO₂ and corresponding Lorentzian distribution of the dye's LUMO for L0 (a), JK2 (b), JK2-T (c) and D102 (d) in their neutral form (1H). The TiO₂ PDOS have been normalized; those corresponding to the sensitizer have been normalized and multiplied by 50; and the Lorentzian distributions have been normalized on the dye's PDOS maximum. Figure adapted from Ref.⁶⁴

The TiO₂ PDOS have basically the same profile of that of the corresponding bare TiO₂ slab, apart from a small upshift (ca. 0.1-0.2 eV) induced by the adsorbed dye (see the CB edge energetic values for the isolated semiconductor (E_{CB}) and for the TiO₂ in the complex ($E_{CB-complex}$) in Table 1).

These energy shifts come out from the combined effect of the electrostatic potential generated by the dye on the TiO₂ surface and of the charge moving from the dye to the TiO₂ by virtue of the dye-semiconductor interactions, as detailed above.⁶² On the other hand, when the dye is bound to the semiconductor, the LUMO tends to have significant spread over a large number of eigenvalues, as shown by the sizable broadenings presented by the dye's LUMO PDOS (green lines in Figure 6). By the Newns-Anderson model, we can calculate the energy of the LUMO for the adsorbed dye and its relative shift with respect to the value in the isolated dye,

Table 1: Calculated CB of the bare TiO₂ at the geometry It has in the complex (E_{CB}), Energy of the LUMO of the dye anchored on the TiO₂ (E_{LUMO}), CB of the TiO₂ when the dye is adsorbed ($E_{CB-complex}$) and Lorentzian Broadening ($\hbar\Gamma$) for the investigated systems in 1H Form. Data from Ref.⁶⁴

Dye	E_{CB} (eV)	$E_{HOMO-complex}$ (eV)	E_{LUMO} (eV)	$E_{CB-complex}$ (eV)	$\hbar\Gamma$ (eV)
L0	-3.999	-5.622	-2.793	-3.845	0.210
JK2	-3.999	-5.105	-3.131	-3.844	0.141
JK2-T	-4.000	-5.013	-3.087	-3.859	0.209
D102	-4.000	-5.191	-2.683	-3.839	0.116

(equation 74), the energetic Lorentzian distribution (Figure 6) and the corresponding broadening (equation 75).

Starting our discussion from the system containing the L0 dye (6a), we observe a sizeable broadening amounting to 0.21 eV, which delivers an electron injection time of about 3 fs, in qualitative agreement with the theoretical and experimental reference data. In particular, this value is comparable with those evaluated by the use of different and more refined theoretical methods (2-10 fs, see Ref.¹⁷¹ and Ref.¹⁷²), for similar organic sensitizers and is certainly less than 200 fs as expected from experimental measurements.^{173,174}

Turning now to the JK2 dye, the plots in Figure 6b show that the sensitizer’s LUMO PDOS is centered at lower energies when compared to that of L0, in line with the LUMO energies of the isolated dyes (-3.00 eV and -2.54 eV for JK2 and L0 respectively). In contrast to what was obtained for L0, the JK2 adsorbed LUMO is mainly localized on the dye states, as evidenced by the largely smaller value of the energetic broadening (0.14 eV), resulting in a 40% increased electron injection time with respect to that computed for L0, consistent with the reference data from the literature.¹⁷¹⁻¹⁷⁴ Despite this, JK2 shows good electron injection properties, as suggested by the high efficiency ($\sim 8\%$) obtained in cells built using this sensitizer.¹⁶⁷ When dealing with the injection rate, two main variables, related to the dye’s molecular structure, have to be considered:¹⁷¹ the electron injection energy (E_{LUMO}), which dictates the driving force, and the percentage of LUMO localized on the anchoring moiety, which dictates the electronic coupling. We can attribute a part of the variations observed in the injection rates to the above discussed shift between the LUMO energies of the two dyes in both the adsorbed and standalone forms. In particular, by a comparison of the Lorentzian distributions with the semiconductor PDOSs, we notice that L0 presents the LUMO in an energetic region where the TiO₂ states are more dense, while the JK2 LUMO is energetically localized close to the CB edge, where there are few semiconductor empty states available for the mixing. Turning to the localization of the dye’s LUMO, the percentage of the LUMO on the anchoring moiety atoms can be obtained by summing the p_i contributions of the LUMO relative to the atoms of the cyanoacrylic group. A similar procedure can be applied also to the dye adsorbed on the semiconductor by performing the sum on a number of complex states containing a unitary contribution of the sensitizer. As expected, L0, in its free protonated form, has about 31% of the LUMO localized in the anchoring moiety while for JK2 this state is more distributed along the molecule and shows a percentage of 24% on the cyanoacrylic group; if we consider the dyes in the complex with the TiO₂, the two percentages increase, but a comparable difference between the two systems still remains (66% for L0 and 51% for JK2). To further elucidate this effect, we investigated, the JK2-T dye, where we twisted by 90° the C-C bond connecting the cyanoacrylic anchoring moiety to the first thiophene ring of the π -spacer; the corresponding PDOSs are reported in Figure 6c. It is worth noting that while the dye’s LUMO energy is almost unaffected by the twisting of the bond (the energy change is only 0.05 eV), the broadening of the LUMO distribution is strongly modified (Figure 6c). By the analysis of the corresponding Lorentzian distribution, we quantified the increase in the broadening, amounting to about 0.07 eV. From these values we then evaluated the injection time for the JK2-T dye, obtaining a value of 3 fs. As the breaking of the conjugation has a negligible effect on the LUMO energy, this large increase in the injection rate can be completely attributed to the increase of the LUMO localization on the anchoring region. As a matter of fact, passing from the planar to the twisted JK2 configuration, the LUMO localization on the cyanoacrylic moiety increases by about 18% and 35% in dye in its free and adsorbed form, respectively.⁶⁴

We conclude with the D102 dye, attached to TiO₂ by a nonconjugated rhodanine-3-acetic anchoring moiety¹⁶⁸ (Figure 4b). The LUMO PDOS maximum (Figure 6d) is energetically localized at higher energies with

respect to that of the other dyes, and a small stabilization (0.07 eV) of the lowest-energy unoccupied state between the free (-2.61 eV) and adsorbed system is obtained. This is indicative of a small coupling between the sensitizer and the semiconductor states. Indeed the calculated energetic broadening is 0.12 eV, yielding an increased injection time of ~ 6 fs. The LUMO component on the carboxylic unit is negligible, as for D102 anchored on TiO_2 , the LUMO localization on the carboxylic group amounts to 12%, significantly smaller than those relative to the other dyes (L0@ TiO_2 , 22%; JK2@ TiO_2 , 17%; JK2-T@ TiO_2 , 26%). Despite this very low localization of the injecting orbital on the anchoring unit, the charge transfer rate, remains in the ultrafast timescale (within 100 fs). These relatively fast injection kinetics can be explained considering the LUMO energetic position, localized in a dense region of TiO_2 states (~ 126 states/eV for the bare semiconductor and ~ 130 states/eV for the TiO_2 in the presence of the sensitizer, Table 1).

3.2.2 TiO_2 Protonation: Energy Level Shifts and Dye-Semiconductor Electronic Coupling

How does TiO_2 protonation modify the relative dye/semiconductor energy level alignment and the electronic coupling? The effect on the injection rates upon surface protonation can be basically attributed to two interplaying factors: (i) the dependence of the TiO_2 DOS and of the dye’s LUMO position on the number of H^+ adsorbed on the surface and (ii) the variation of the coupling matrix elements between the sensitizer and the semiconductor. Here we go beyond the Newns-Anderson model, by directly calculating the electronic coupling between the localized dye’s and semiconductor’s states.

The results for the L0@ TiO_2 system in all the modeled protonation forms (from 1H to 5H) are reported in Figure 7, while those for the JK2 and D102 dyes in both 1H and 5H forms investigated are displayed in Figure 8.

In Table 2 we collect some relevant quantities extracted upon the diabaticization step: the energy of the diabatic TiO_2 CB; the dye’s HOMO and LUMO, with the associated HOMO-LUMO gap; and the injection function $\Gamma(E)$ evaluated at the energy of both diabatic and Lorentzian (NA) LUMO, which is also reported for the sake of completeness.

Table 2: Calculated Energies (Electronvolts) of Diabatic TiO_2 Conduction Band (CB_{DIA}), Dye’s HOMO and LUMO and HOMO-LUMO Gap (GAP_{DIA}), Injection Function ($\Gamma(E)$) Evaluated at the Energy of Both Diabatic (Γ^{DIA} , LUMO_{DIA}) and Lorentzian (Γ^{DIA} , LUMO_{NA}) LUMO, and Lorentzian LUMO (LUMO_{NA}). Reprinted with permission from (Ronca, E.; Marotta, G.; Pastore, M; De Angelis, F. Effect of Sensitizer Structure and TiO_2 Protonation on Charge Generation in Dye-Sensitized Solar Cells *J. Phys. Chem. C*, **2014**, *118*, 16927-16940). Copyright (2014) American Chemical Society.

H^+	CB_{DIA}	LUMO_{DIA}	HOMO_{DIA}	GAP_{DIA}	$\Gamma^{DIA}(\text{LUMO}_{DIA})$	LUMO_{NA}	$\Gamma^{DIA}(\text{LUMO}_{NA})$
L0							
1H	-3.830	-2.643	-5.603	2.959	0.220	-2.793	0.247
2H	-4.132	-2.762	-5.685	2.923	0.327	-2.945	0.410
3H	-4.042	-2.826	-5.721	2.895	0.199	-3.012	0.271
4H	-4.132	-2.921	-5.783	2.862	0.279	-3.120	0.377
5H	-4.229	-2.991	-5.836	2.845	0.302	-3.190	0.392
JK2							
1H	-3.846	-3.025	-5.100	2.074	0.231	-3.131	0.233
5H	-4.220	-3.337	-5.214	1.877	0.375	-3.484	0.401
D102							
1H	-3.999	-2.593	-5.188	2.596	0.003	-2.683	0.003
5H	-4.391	-2.699	-5.188	2.489	0.005	-2.815	0.006

Let us start by discussing the case of L0: as is apparent from the plots in Figure 7, we observe a very regular increase in the electronic coupling at lower energies as the number of protons on the surface increases, with the only exception being the 2H case, which shows an exaggerated increment in the low energy region, possibly due to the fact that the only positive charge is located at one of the cluster corners. As higher energies are considered, the coupling values progressively tend to decrease. The $\Gamma(E)$ functions (obtained by the product of the square of the electronic coupling and the DOS) show a pronounced maximum in correspondence of the TiO_2 CB edge region, where the coupling is higher. The progressive increasing of the protonation degree yields a sizable energetic shift of the Γ distribution maximum, which is clearly related to semiconductor CB edge

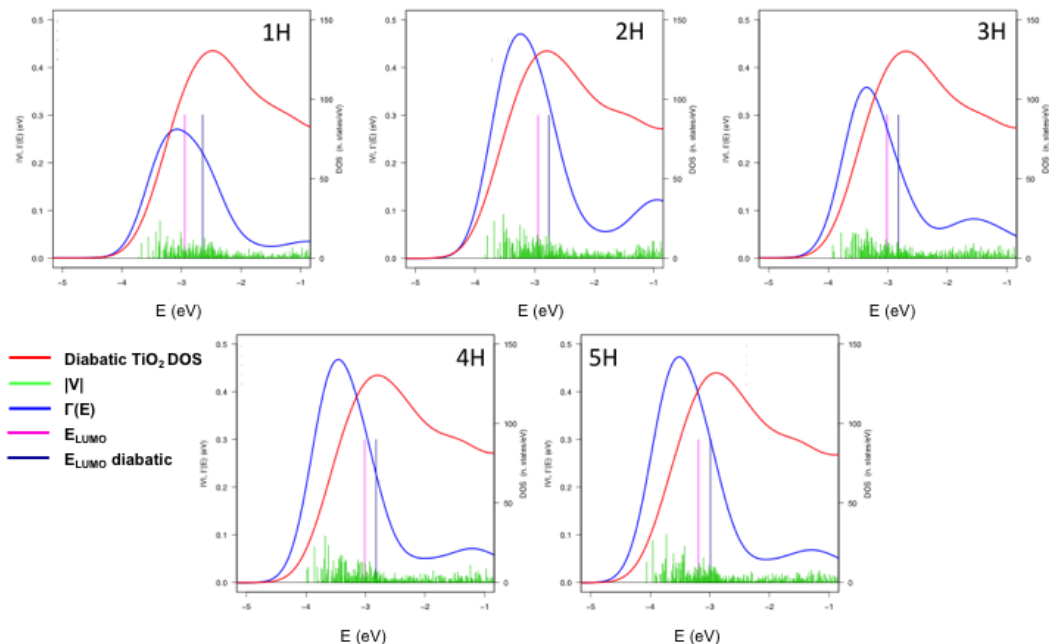


figure 7: Absolute value of the coupling matrix elements (V_{dk}) between the dye LUMO and the TiO_2 virtual states (green sticks), injection broadening $\Gamma(E)$ function (blue line), and DOS relative to the virtual localized (diabatic) orbital of the semiconductor (red line) for L0@TiO_2 in different protonation forms as a function of the energy (E). For each system the magenta and blue vertical lines represent the energetic position of the adsorbed dye LUMOs evaluated as the maximum of the Newns-Anderson Lorentzian distribution and as the energy of the localized orbital more similar to the sensitizer's first virtual state, respectively. The Gaussian broadening used to reproduce both the TiO_2 DOS and the $\Gamma(E)$ function is equal to 0.3 eV. Figure adapted from Ref.⁶⁴

lowering (0.1 eV per proton added). By extracting the value of $\Gamma(E)$ at the sensitizer's LUMO energy, one can estimate the charge injection rate from the dye to the semiconductor. It is worthwhile to stress that the position of the dye LUMO can be evaluated in two different ways: in the adiabatic picture, as the energy of the Newns-Anderson Lorentzian distribution maximum (LUMO_{NA} , magenta sticks in Figures 7 and 8) and, in the diabatic framework, as the energy of the localized orbital corresponding to the dye LUMO (dark blue sticks in Figures 7 and 8). We then extracted the Γ function intensity in the dye LUMO range, obtaining a value of about 0.22-0.25 eV (corresponding to about 3 fs) for the 1H form and 0.30-0.39 eV (~ 2 fs) for the 5H case. Similar conclusions can be drawn also for the system containing the JK2 dye (upper panels in Figure 8). Comparing the $\Gamma(E)$ curves with those of the L0 dye, we can immediately notice a lowering of the injection rates (about 0.1 eV at the maxima energetic position) in the whole energy range and for both the protonation, imputable to the smaller spatial localization of the LUMO on the anchoring unit found in JK2 compared to L0. This trend is consistent with the results provided by the Newns-Anderson model and discussed in the previous section. However, by extracting the $\Gamma(E)$ function in the dye LUMO range, we obtain injection rate values of 0.23 eV for the 1H form and 0.37-0.40 eV for the 5H case, which result in values somewhat larger than those calculated for the corresponding L0 systems. This is clearly the result of a more favorable energetic position of the dye's LUMO, which, lying at lower energies, can inject into the CB states for which the electronic coupling is higher (i.e., the LUMO position falls in the region where the $\Gamma(E)$ function shows the maximum).

Turning now to the nonconjugated D102 dye, comparing the injection rates in Table 2 with those reported in

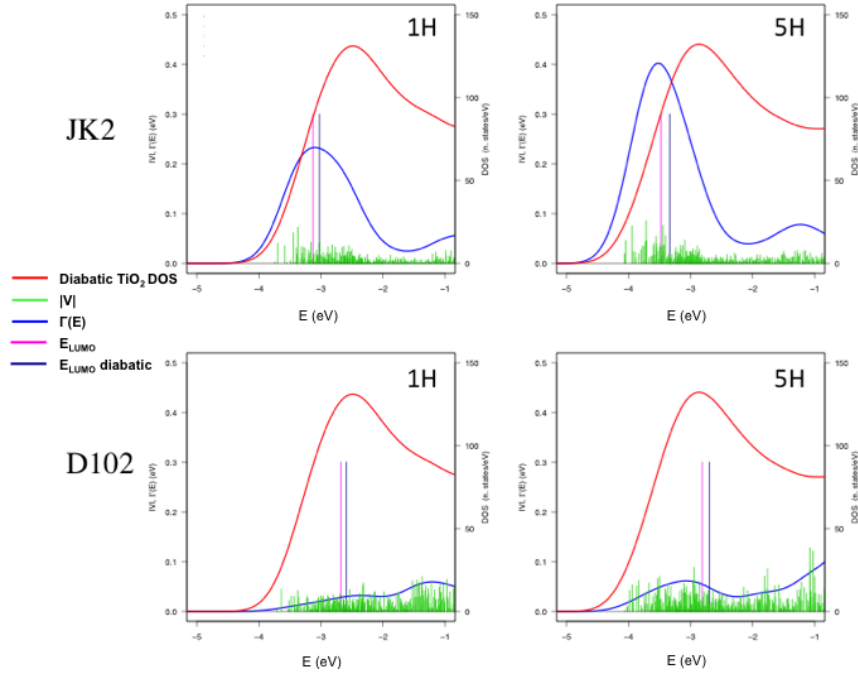


figure 8: Absolute value of the coupling matrix elements (V_{dk}) between the dye LUMO and the TiO₂ virtual states (green sticks), injection broadening $\Gamma(E)$ function (blue line), and DOS relative to the virtual localized (diabatic) orbital of the semiconductor (red line) for the JK2@TiO₂ and D102@TiO₂ systems in the 1H (left panels) and 5H (right panels) protonation form as a function of the energy (E). For each system, the magenta and blue vertical lines represent the energetic position of the adsorbed dye LUMOs evaluated as the maximum of the Newns-Anderson Lorentzian distribution and as the energy of the localized orbital more similar to the sensitizer first virtual state, respectively. The Gaussian broadening used to reproduce both the TiO₂ DOS and the $\Gamma(E)$ function is equal to 0.3 eV. Note that in the case of the D102 dye (bottom panels) both the coupling matrix elements (V_{dk}) and the $\Gamma(E)$ function were multiplied by 10. Figure adapted from Ref.⁶⁴

Table 1, we observe a substantial disagreement between the results provided by the two approaches. In fact, by considering the explicit coupling between the LUMO and the CB states, we obtain electronic coupling values of 0.003 (1H) and 0.005 eV (5H), whereas the values obtained by the Lorentzian broadening are 0.12 (1H) and 0.16 eV (5H). While the diabatic results are clearly consistent with the not conjugated structure of the dye and with the negligible localization of the dye's LUMO on the carboxylate anchoring group, the broadening estimated in the Newns-Anderson model by means of a Mulliken population analysis is evidently sensitive to the basis set quality choice, a well-know drawback of this kind of electron population scheme, where the electron density is projected onto the basis set.¹⁷⁵

Final remarks concern the effect of surface protonation on the dye and TiO₂ energy levels: comparing the CB and LUMO energy levels for the different dyes, reported in Table 2, one can notice that while the extent of the CB_{DIA} down-shift as the number of protons increases does not depend on the particular dye adsorbed, different dyes show different down-shifts of the LUMO going from the 1H to 5H forms. While the stabilization of the LUMO (both diabatic and NA) is in the range 0.35-0.39 eV, comparable to the ca. 0.40 eV shift of the CB edge, we observe a sizeably smaller stabilization of the D102 LUMO, amounting to about 0.1 eV. This is clearly the consequence of the different electronic structure of the interface: the energy levels of the conjugated dyes (L0 and JK2) are more strongly perturbed by the surface protonation, and the stabilization of the TiO₂ CB edge translates into a similar stabilization of the dye's LUMO, while the LUMO of the uncoupled D102 dye is practically unaffected by what happens to the TiO₂ DOS. As a consequence of the progressive charge accumulation on the surface, also the dye's HOMO turns out to be stabilized in the case of the conjugated dyes:

in the shorter L0 system, where the ground-state electronic charge can be more effectively transferred to the protonated TiO_2 ,⁶² the down-shift amounts to 0.23 eV, whereas in the longer JK2 dye, the HOMO stabilization is about 0.1 eV. For the same reasons, the D102 HOMO is practically unchanged upon TiO_2 protonation. The different HOMO and LUMO energy shifts with surface protonation lead to an overall reduction of the dye’s HOMO-LUMO gap (see Table 2) with an increase in the number of adsorbed protons. The entity of such HOMO-LUMO gap variation is clearly strongly dependent on the electronic structure of the dye.

Summarizing, high injection rates come out from the combination of high electronic coupling values of the dye’s LUMO with the TiO_2 CB states and high density of acceptor states. Therefore, maximizing the LUMO’s localization on the anchoring unit, favoring the electronic coupling, and shifting its position to relatively higher energies, where the TiO_2 DOS is denser, appear as optimal design rules to increase the electron injection efficiency. Concerning the substrate protonation, on the other side, the present results demonstrate that the presence of protons on the TiO_2 surface, while shifting of both the semiconductor CB and dye’s LUMO energetic positions, increases the injection rate mainly because of the increase in the coupling matrix elements, in particular with the substrate states in the lower energy region.

4 Conclusion

In the first part of this book chapter we revisited the theoretical elements necessary to elaborate qualitative and quantitative strategies for probing the structure, nature and locality of molecular exciton from excited states quantum-chemical calculations. For the qualitative analyses we exposed how the direct manipulation of quantum state charge densities can provide density functions leading to a clear picture of the transition. We also showed that as an alternative to the direct transposition of density matrices into the Euclidean space, one can also perform some algebraic operations on these matrices in order to obtain the hole/particle density matrices, called detachment/attachment density matrices. The direct inspection of the canonical orbitals was then exposed, as well as the possibility to derive two different orbitals sets (natural difference orbitals, natural transition orbitals) for excited states composed as a linear combination of singly-excited Slater determinants obtained from a single reference ground state wave function. In the special case of RPA, TDHF and TDDFT methods we also gave the definition of some transition orbitals (the projected natural transition orbitals and the canonical transition orbitals). On the other hand, quantitative analyses can also be classified according to the type of information provided: we exposed fragment-based analyses that assess the changes specific to a molecular fragment, global strategies which take into account the whole electronic system to provide an information related to the behavior of the entire molecule upon light absorption. Quantitative insights related to the statistical properties of the hole/particle distribution, or to its entanglement for example, were also reported. In the second part we, instead, discuss how the different electronic structure of the dye and dye-anchored metal oxide substrates directly influences the energy levels line-up at the interface, as well as the ground and excited state charge distribution and finally the electronic coupling and electron injection rates. In the case of electronically conjugated dye- TiO_2 interface, the substrate conduction band is up shifted, yielding higher V_{oc} , by a combined electrostatic (about 40%) and ground state dye \rightarrow semiconductor charge transfer (about 60%) effect. On the other hand, in the case of the electronically decoupled dye-NiO interface, the interfacial electrostatic is the dominant component ruling the relative dye’s HOMO metal oxide VB energy levels line-up. The dependence of the injection rate on the dye molecular and electronic structure has been investigated by the simple Newns-Anderson model, showing that changes in the units constituting the sensitizer (without altering the conjugation) produces variations both on the energy and on the spatial localization of the injecting LUMO orbital. This clearly reflects on the energetic alignment between the dye and TiO_2 states and on the coupling between the interacting species, with inevitable consequences on the corresponding injection rates. As a final example we have reviewed the effects produced by a shift of the TiO_2 CB edge, simulated by adsorbing an increasing number of protons on the semiconductor surface, on the calculated injection rates. To do that, use was made of a diabatic-like treatment, which provided us with the coupling matrix elements between the injecting LUMO orbital and the semiconductor CB acceptor orbitals. Addition of protons on the semiconductor surface, while producing a consistent shift of both the TiO_2 CB and dye LUMO energetic positions, influences the injection rate mainly through the variations generated in the electronic coupling.

Acknowledgements

MP thanks COHESION and ANR-HELIOSH2 for financial support.

References

- [1] M. Grätzel, "Dye-sensitized solar cells," *J. Photochem. Photobiol. C: Photochem. Rev.*, vol. 4, no. 2, pp. 145–153, 2003.
- [2] M. Grätzel, "Recent advances in sensitized mesoscopic solar cells," *Acc. Chem. Res.*, vol. 42, no. 11, pp. 1788–1798, 2009.
- [3] A. Hagfeldt, G. Boschloo, L. Sun, L. Kloo, and H. Pettersson, "Dye-sensitized solar cells," *Chem. Rev.*, vol. 110, no. 11, pp. 6595–6663, 2010.
- [4] L. Alibabaei, M. K. Brennaman, M. R. Norris, B. Kalanyan, W. Song, M. D. Losego, J. J. Concepcion, R. A. Binstead, G. N. Parsons, and T. J. Meyer, "Solar water splitting in a molecular photoelectrochemical cell," *Proc. Natl. Acad. Sci.*, vol. 110, no. 50, pp. 20008–20013, 2013.
- [5] M. G. Walter, E. L. Warren, J. R. McKone, S. W. Boettcher, Q. Mi, E. A. Santori, and N. S. Lewis, "Solar water splitting cells," *Chem. Rev.*, vol. 110, no. 11, pp. 6446–6473, 2010.
- [6] W. J. Youngblood, S.-H. A. Lee, K. Maeda, and T. E. Mallouk, "Visible light water splitting using dye-sensitized oxide semiconductors," *Acc. Chem. Res.*, vol. 42, no. 12, pp. 1966–1973, 2009.
- [7] Z. Yu, F. Li, and L. Sun, "Recent advances in dye-sensitized photoelectrochemical cells for solar hydrogen production based on molecular components," *Energy Environ. Sci.*, vol. 8, pp. 760–775, 2015.
- [8] B. O'Regan and M. Grätzel, "A low-cost, high-efficiency solar cell based on dye-sensitized colloidal TiO_2 films," *Nature*, vol. 353, pp. 737–740, 1991.
- [9] J. He, H. Lindström, A. Hagfeldt, and S.-E. Lindquist, "Dye-sensitized nanostructured p-type nickel oxide film as a photocathode for a solar cell," *J. Phys. Chem. B*, vol. 103, no. 42, pp. 8940–8943, 1999.
- [10] M. Borgström, E. Blart, G. Boschloo, E. Mukhtar, A. Hagfeldt, L. Hammarström, and F. Odobel, "Sensitized hole injection of phosphorus porphyrin into nio: Toward new photovoltaic devices," *J. Phys. Chem. B*, vol. 109, no. 48, pp. 22928–22934, 2005.
- [11] F. Odobel, Y. Pellegrin, E. A. Gibson, A. Hagfeldt, A. L. Smeigh, and L. Hammarström, "Recent advances and future directions to optimize the performances of p-type dye-sensitized solar cells," *Coord. Chem. Rev.*, vol. 256, no. 21 - 22, pp. 2414 – 2423, 2012.
- [12] M. K. Brennaman, R. J. Dillon, L. Alibabaei, M. K. Gish, C. J. Dares, D. L. Ashford, R. L. House, G. J. Meyer, J. M. Papanikolas, and T. J. Meyer, "Finding the way to solar fuels with dye-sensitized photoelectrosynthesis cells," *J. Am. Chem. Soc.*, vol. 138, no. 40, pp. 13085–13102, 2016.
- [13] M. Pastore, A. Selloni, S. Fantacci, and F. Angelis, "Electronic and optical properties of dye-sensitized TiO_2 interfaces," *Top. Curr. Chem.*, pp. 1–45, Springer Berlin Heidelberg, 2014.
- [14] M. Pastore, T. Duchanois, L. Liu, A. Monari, X. Assfeld, S. Haacke, and P. C. Gros, "Interfacial charge separation and photovoltaic efficiency in $\text{Fe}(\text{II})$ -carbene sensitized solar cells," *Phys. Chem. Chem. Phys.*, vol. 18, pp. 28069–28081, 2016.
- [15] M. Pastore, S. Fantacci, and F. De Angelis, "Modeling excited states and alignment of energy levels in dye-sensitized solar cells: Successes, failures, and challenges," *J. Phys. Chem. C*, vol. 117, no. 8, pp. 3685–3700, 2013.

- [16] E. Ronca, C. Angeli, L. Belpassi, F. De Angelis, F. Tarantelli, and M. Pastore, "Density relaxation in time-dependent density functional theory: Combining relaxed density natural orbitals and multireference perturbation theories for an improved description of excited states," *J. Chem. Theory Comput.*, vol. 10, no. 9, pp. 4014–4024, 2014.
- [17] F. Labat, T. Le Bahers, I. Ciofini, and C. Adamo, "First-principles modeling of dye-sensitized solar cells: Challenges and perspectives," *Acc. Chem. Res.*, vol. 45, no. 8, pp. 1268–1277, 2012.
- [18] D. Jacquemin, E. A. Perpète, I. Ciofini, and C. Adamo, "Accurate simulation of optical properties in dyes," *Acc. Chem. Res.*, vol. 42, pp. 326–334, Feb. 2009.
- [19] F. Plasser and H. Lischka, "Analysis of excitonic and charge transfer interactions from quantum chemical calculations," *J. Chem. Theory Comput.*, vol. 8, pp. 2777–2789, Aug. 2012.
- [20] F. Plasser, M. Wormit, and A. Dreuw, "New tools for the systematic analysis and visualization of electronic excitations. i. formalism," *J. Chem. Phys.*, vol. 141, p. 024106, July 2014.
- [21] F. Plasser, S. A. Bäßler, M. Wormit, and A. Dreuw, "New tools for the systematic analysis and visualization of electronic excitations. ii. applications," *J. Chem. Phys.*, vol. 141, p. 024107, July 2014.
- [22] S. A. Bäßler, F. Plasser, M. Wormit, and A. Dreuw, "Exciton analysis of many-body wave functions: Bridging the gap between the quasiparticle and molecular orbital pictures," *Phys. Rev. A*, vol. 90, p. 052521, Nov. 2014.
- [23] S. A. Mewes, F. Plasser, and A. Dreuw, "Communication: Exciton analysis in time-dependent density functional theory: How functionals shape excited-state characters," *J. Chem. Phys.*, vol. 143, no. 17, p. 171101, 2015.
- [24] F. Plasser, B. Thomitzni, S. A. Bäßler, J. Wenzel, D. R. Rehn, M. Wormit, and A. Dreuw, "Statistical analysis of electronic excitation processes: Spatial location, compactness, charge transfer, and electron-hole correlation," *J. Comp. Chem.*, vol. 36, no. 21, pp. 1609–1620, 2015.
- [25] J. Wenzel and A. Dreuw, "Physical Properties, Exciton Analysis, and Visualization of Core-Excited States: An Intermediate State Representation Approach," *J. Chem. Theory Comput.*, vol. 12, pp. 1314–1330, Mar. 2016.
- [26] F. Plasser, "Entanglement entropy of electronic excitations," *J. Chem. Phys.*, vol. 144, no. 19, p. 194107, 2016.
- [27] S. Mai, F. Plasser, J. Dorn, M. Fumanal, C. Daniel, and L. Gonzalez, "Quantitative wave function analysis for excited states of transition metal complexes," *Coord. Chem. Rev.*, vol. 361, pp. 74–97, Apr. 2018. arXiv: 1711.10707.
- [28] T. Etienne, "Transition matrices and orbitals from reduced density matrix theory," *J. Chem. Phys.*, vol. 142, no. 24, p. 244103, 2015.
- [29] T. Etienne, "Theoretical Insights into the Topology of Molecular Excitons from Single-Reference Excited States Calculation Methods," *Excitons*, Sergei L. Pyshkin Ed., InTech, 2018, doi 10.5772/intechopen.70688.
- [30] B. Dedeoglu, A. Monari, T. Etienne, V. Aviyente, and A. S. Ozen, "Detection of nitroaromatic explosives based on fluorescence quenching of silafluorene- and silole-containing polymers: A time-dependent density functional theory study," *J. Phys. Chem. C*, Sept. 2014.
- [31] T. Etienne, H. Gattuso, A. Monari, and X. Assfeld, "Qm/mm modeling of harmaline cation fluorescence spectrum in water solution and interacting with dna," *Comput. Theor. Chem.*, vol. 1040, pp. 367–372, 2014.

- [32] T. Etienne, H. Gattuso, C. Michaux, A. Monari, X. Assfeld, and E. A. Perpète, “Fluorene-imidazole dyes excited states from first-principles calculations Topological insights,” *Theor. Chem. Acc.*, vol. 135, pp. 1–11, Apr. 2016.
- [33] E. K.-L. Ho, T. Etienne, and B. Lasorne, “Vibronic properties of para-polyphenylene ethynyls: Td-dft insights,” *J. Chem. Phys.*, vol. 146, no. 16, p. 164303, 2017.
- [34] T. Etienne, T. Duchanois, M. Beley, E. A. Perpète, P. Gros, A. Monari, and X. Assfeld *In Preparation*.
- [35] T. Etienne, L. Chbib, C. Michaux, E. A. Perpète, X. Assfeld, and A. Monari, “All-organic chromophores for dye-sensitized solar cells: A theoretical study on aggregation,” *Dyes Pigm.*, vol. 101, pp. 203–211, Feb. 2014.
- [36] T. Duchanois, T. Etienne, M. Beley, X. Assfeld, E. A. Perpète, A. Monari, and P. C. Gros, “Heteroleptic pyridyl-carbene iron complexes with tuneable electronic properties,” *Eur. J. Inorg. Chem.*, vol. 2014, pp. 3747–3753, Aug. 2014.
- [37] T. Duchanois, T. Etienne, C. Cebrián, L. Liu, A. Monari, M. Beley, X. Assfeld, S. Haacke, and P. C. Gros, “An iron-based photosensitizer with extended excited-state lifetime: Photophysical and photovoltaic properties,” *Eur. J. Inorg. Chem.*, vol. 2015, no. 14, pp. 2469–2477, 2015.
- [38] L. Liu, T. Duchanois, T. Etienne, A. Monari, M. Beley, X. Assfeld, S. Haacke, and P. C. Gros, “A new record excited state 3mlct lifetime for metalorganic iron(ii) complexes,” *Phys. Chem. Chem. Phys.*, vol. 18, pp. 12550–12556, 2016.
- [39] R. L. Martin, “Natural transition orbitals,” *J. Chem. Phys.*, vol. 118, no. 11, pp. 4775–4777, 2003.
- [40] E. R. Batista and R. L. Martin, “Natural transition orbitals,” *Encyclopedia of Computational Chemistry*, P. Ragué Schleyer, N. L. Allinger, T. Clark, J. Gasteiger, P. A. Kollman, H. F. Schaefer, P. R. Schreiner, W. Thiel, W. L. Jorgensen and R. C. Glen Eds., American Cancer Society, 2004.
- [41] A. Dreuw and M. Head-Gordon, “Single-reference ab initio methods for the calculation of excited states of large molecules,” *Chem. Rev.*, vol. 105, pp. 4009–4037, Nov. 2005.
- [42] I. Mayer, “Using singular value decomposition for a compact presentation and improved interpretation of the cis wave functions,” *Chem. Phys. Lett.*, vol. 437, pp. 284–286, Apr. 2007.
- [43] P. R. Surján, “Natural orbitals in cis and singular-value decomposition,” *Chem. Phys. Lett.*, vol. 439, pp. 393–394, May 2007.
- [44] F. Furche, “On the density matrix based approach to time-dependent density functional response theory,” *J. Chem. Phys.*, vol. 114, pp. 5982–5992, Apr. 2001.
- [45] A. V. Luzanov and O. A. Zhikol, “Electron invariants and excited state structural analysis for electronic transitions within cis, rpa, and tddft models,” *Int. J. Quantum Chem.*, vol. 110, no. 4, pp. 902–924, 2010.
- [46] A. V. Luzanov and V. F. Pedash, “Interpretation of excited states using charge-transfer numbers,” *Theor. Exp. Chem.*, vol. 15, pp. 338–341, July 1980.
- [47] Yonghui Li; and C.A. Ullrich, “Time-dependent transition density matrix,” *Chem. Phys.*, vol. 391, no. 1, pp. 157–163, 2001.
- [48] S. Tretiak and S. Mukamel, “Density matrix analysis and simulation of electronic excitations in conjugated and aggregated molecules,” *Chem. Rev.*, vol. 102, pp. 3171–3212, Sept. 2002.
- [49] C. Wu, S. V. Malinin, S. Tretiak, and V. Y. Chernyak, “Exciton scattering approach for branched conjugated molecules and complexes. iii. applications,” *J. Chem. Phys.*, vol. 129, no. 17, p. 174113, 2008.

- [50] S. Tretiak, K. Igumenshchev, and V. Chernyak, "Exciton sizes of conducting polymers predicted by time-dependent density functional theory," *Physical review B*, vol. 71, no. 3, p. 033201, 2005.
- [51] M. Head-Gordon, A. M. Grana, D. Maurice, and C. A. White, "Analysis of electronic transitions as the difference of electron attachment and detachment densities," *J. Phys. Chem.*, vol. 99, p. 14261, 1995.
- [52] M. Pastore, X. Assfeld, E. Mosconi, A. Monari, and T. Etienne, "Unveiling the nature of post-linear response z-vector method for time-dependent density functional theory," *J. Chem. Phys.*, vol. 147, no. 2, p. 024108, 2017.
- [53] M. J. G. Peach, P. Benfield, T. Helgaker, and D. J. Tozer, "Excitation energies in density functional theory: an evaluation and a diagnostic test," *J. Chem. Phys.*, vol. 128, p. 044118, Jan. 2008.
- [54] T. Le Bahers, C. Adamo, and I. Ciofini, "A qualitative index of spatial extent in charge-transfer excitations," *J. Chem. Theory Comput.*, vol. 7, pp. 2498–2506, Aug. 2011.
- [55] G. García, C. Adamo, and I. Ciofini, "Evaluating push–pull dye efficiency using td-dft and charge transfer indices," *Phys. Chem. Chem. Phys.*, Oct. 2013.
- [56] C. A. Guido, P. Cortona, B. Mennucci, and C. Adamo, "On the metric of charge transfer molecular excitations: A simple chemical descriptor," *J. Chem. Theory Comput.*, vol. 9, no. 7, pp. 3118–3126, 2013.
- [57] T. Etienne, X. Assfeld, and A. Monari, "Toward a quantitative assessment of electronic transitions' charge-transfer character," *J. Chem. Theory Comput.*, vol. 10, pp. 3896–3905, Sept. 2014.
- [58] T. Etienne, X. Assfeld, and A. Monari, "New insight into the topology of excited states through detachment/attachment density matrices-based centroids of charge," *J. Chem. Theory Comput.*, vol. 10, pp. 3906–3914, Sept. 2014.
- [59] C. A. Guido, P. Cortona, and C. Adamo, "Effective electron displacements: A tool for time-dependent density functional theory computational spectroscopy," *J. Chem. Phys.*, vol. 140, p. 104101, Mar. 2014.
- [60] T. Etienne, "Probing the locality of excited states with linear algebra," *J. Chem. Theory Comput.*, pp. 1692–1699, feb 2015.
- [61] M. Savarese, C. A. Guido, E. Brémond, I. Ciofini, and C. Adamo, "Metrics for Molecular Electronic Excitations: A Comparison between Orbital- and Density-Based Descriptors," *J. Phys. Chem. A*, vol. 121, pp. 7543–7549, Oct. 2017.
- [62] E. Ronca, M. Pastore, L. Belpassi, F. Tarantelli, and F. De Angelis, "Influence of the dye molecular structure on the tio2 conduction band in dye-sensitized solar cells: disentangling charge transfer and electrostatic effects," *Energy Environ. Sci.*, vol. 6, pp. 183–193, 2013.
- [63] S. Piccinin, D. Rocca, and M. Pastore, "Role of solvent in the energy level alignment of dye-sensitized nio interfaces," *J. Phys. Chem. C*, vol. 121, no. 40, pp. 22286–22294, 2017.
- [64] E. Ronca, G. Marotta, M. Pastore, and F. De Angelis, "Effect of sensitizer structure and tio2 protonation on charge generation in dye-sensitized solar cells," *J. Phys. Chem. C*, vol. 118, no. 30, pp. 16927–16940, 2014.
- [65] D. Jacquemin, "The CT package," <http://www.sciences.univ-nantes.fr/CEISAM/erc/marches/?p=973>, consulted July 2018.
- [66] F. Plasser, "TheoDORE," <http://theodore-qc.sourceforge.net>, consulted July 2018.
- [67] X. Assfeld, A. Monari, T. Very, and T. Etienne, "Nancy-ex 2.0," <https://sourceforge.net/projects/nancyex/>, consulted July 2018.

- [68] T. Etienne, “The taeles software,” taeles.wordpress.com, consulted July 2018.
- [69] E. Ronca, M. Pastore, L. Belpassi, F. D. Angelis, C. Angeli, R. Cimiraglia, and F. Tarantelli, “Charge-displacement analysis for excited states,” *J. Chem. Phys.*, vol. 140, p. 054110, Feb. 2014.
- [70] E. Ronca, C. Angeli, L. Belpassi, F. De Angelis, F. Tarantelli, and M. Pastore, “Density relaxation in time-dependent density functional theory: Combining relaxed density natural orbitals and multireference perturbation theories for an improved description of excited states,” *J. Chem. Theory Comput.*, July 2014.
- [71] A. T. Amos and G. G. Hall, “Single determinant wave functions,” *Proc. R. Soc. Lond. A*, vol. 263, pp. 483–493, Oct. 1961.
- [72] H. Ehrenreich and M. H. Cohen, “Self-consistent field approach to the many-electron problem,” *Phys. Rev.*, vol. 115, pp. 786–790, Aug 1959.
- [73] S. Hirata, M. Head-Gordon, and R. J. Bartlett, “Configuration interaction singles, time-dependent hartree–fock, and time-dependent density functional theory for the electronic excited states of extended systems,” *J. Chem. Phys.*, vol. 111, no. 24, pp. 10774–10786, 1999.
- [74] S. Hirata and M. Head-Gordon, “Time-dependent density functional theory within the tamm–dancoff approximation,” *Chem. Phys. Lett.*, vol. 314, pp. 291–299, Dec. 1999.
- [75] M. E. Casida in *Theoretical and Computational Chemistry* (J. M. Seminario, ed.), vol. 4 of *Recent Developments and Applications of Modern Density Functional Theory*, pp. 391–439, Elsevier, 1996.
- [76] M. E. Casida, “Time-dependent density-functional theory for molecules and molecular solids,” *J. Mol. Struct. THEOCHEM*, vol. 914, pp. 3–18, Nov. 2009.
- [77] X. Gui, C. Holzer, and W. Klopper, “Accuracy Assessment of GW Starting Points for Calculating Molecular Excitation Energies Using the Bethe–Salpeter Formalism,” *J. Chem. Theory Comput.*, vol. 14, pp. 2127–2136, Apr. 2018.
- [78] S. P. A. Sauer, *Molecular Electromagnetism: A Computational Chemistry Approach*. OUP Oxford, Aug. 2011. Google-Books-ID: q2WvqTdP7q8C.
- [79] K. S. Gupta, J. Zhang, G. Marotta, M. A. Reddy, S. P. Singh, A. Islam, L. Han, F. D. Angelis, M. Chandrasekharam, and M. Pastore, “Effect of the anchoring group in the performance of carbazole-phenothiazine dyads for dye-sensitized solar cells,” *Dyes Pigm.*, vol. 113, pp. 536 – 545, 2015.
- [80] L. Lasser, E. Ronca, M. Pastore, F. De Angelis, J. Cornil, R. Lazzaroni, and D. Beljonne, “Energy level alignment at titanium oxide-dye interfaces: Implications for electron injection and light harvesting,” *J. Phys. Chem. C*, vol. 119, no. 18, pp. 9899–9909, 2015.
- [81] J. Calbo, M. Pastore, E. Mosconi, E. Orti, and F. De Angelis, “Computational modeling of single- versus double-anchoring modes in di-branched organic sensitizers on tio2 surfaces: structural and electronic properties,” *Phys. Chem. Chem. Phys.*, vol. 16, pp. 4709–4719, 2014.
- [82] C. Anselmi, E. Mosconi, M. Pastore, E. Ronca, and F. De Angelis, “Adsorption of organic dyes on tio2 surfaces in dye-sensitized solar cells: interplay of theory and experiment,” *Phys. Chem. Chem. Phys.*, vol. 14, pp. 15963–15974, 2012.
- [83] V. Shklover, Y. E. Ovchinnikov, L. S. Braginsky, S. M. Zakeeruddin, and M. Grätzel, “Structure of organic/inorganic interface in assembled materials comprising molecular components. crystal structure of the sensitizer bis[(4,4′-carboxy-2,2′-bipyridine)(thiocyanato)]ruthenium(ii),” *Chem. Mater.*, vol. 10, no. 9, pp. 2533–2541, 1998.

- [84] F. De Angelis, S. Fantacci, A. Selloni, M. Grätzel, and M. K. Nazeeruddin, "Influence of the sensitizer adsorption mode on the open-circuit potential of dye-sensitized solar cells," *Nano Lett.*, vol. 7, no. 10, pp. 3189–3195, 2007.
- [85] F. Schiffmann, J. VandeVondele, J. Hutter, R. Wirz, A. Urakawa, and A. Baiker, "Protonation-dependent binding of ruthenium bipyridyl complexes to the anatase(101) surface," *J. Phys. Chem. C*, vol. 114, no. 18, pp. 8398–8404, 2010.
- [86] F. De Angelis, S. Fantacci, A. Selloni, M. K. Nazeeruddin, and M. Grätzel, "First-principles modeling of the adsorption geometry and electronic structure of ru(ii) dyes on extended tio2 substrates for dye-sensitized solar cell applications," *J. Phys. Chem. C*, vol. 114, no. 13, pp. 6054–6061, 2010.
- [87] N. Martsinovich, D. R. Jones, and A. Troisi, "Electronic structure of tio2 surfaces and effect of molecular adsorbates using different dft implementations," *J. Phys. Chem. C*, vol. 114, no. 51, pp. 22659–22670, 2010.
- [88] P. Persson, R. Bergström, and S. Lunell, "Quantum chemical study of photoinjection processes in dye-sensitized tio2 nanoparticles," *J. Phys. Chem. B*, vol. 104, no. 44, pp. 10348–10351, 2000.
- [89] A. Vittadini, A. Selloni, F. P. Rotzinger, and M. Grätzel, "Formic acid adsorption on dry and hydrated tio2 anatase (101) surfaces by dft calculations," *J. Phys. Chem. B*, vol. 104, no. 6, pp. 1300–1306, 2000.
- [90] F. Labat, I. Ciofini, H. P. Hratchian, M. J. Frisch, K. Raghavachari, and C. Adamo, "Insights into working principles of ruthenium polypyridyl dye-sensitized solar cells from first principles modeling," *J. Phys. Chem. C*, vol. 115, no. 10, pp. 4297–4306, 2011.
- [91] F. Labat, T. Le Bahers, I. Ciofini, and C. Adamo, "First-principles modeling of dye-sensitized solar cells: Challenges and perspectives," *Acc. Chem. Res.*, vol. 45, no. 8, pp. 1268–1277, 2012.
- [92] E. Mosconi, A. Selloni, and F. De Angelis, "Solvent effects on the adsorption geometry and electronic structure of dye-sensitized tio2: A first-principles investigation," *J. Phys. Chem. C*, vol. 116, no. 9, pp. 5932–5940, 2012.
- [93] G. Rothenberger, D. Fitzmaurice, and M. Grätzel, "Spectroscopy of conduction band electrons in transparent metal oxide semiconductor films: optical determination of the flatband potential of colloidal titanium dioxide films," *J. Phys. Chem.*, vol. 96, no. 14, pp. 5983–5986, 1992.
- [94] B. O'Regan, M. Grätzel, and D. Fitzmaurice, "Optical electrochemistry i: steady-state spectroscopy of conduction-band electrons in a metal oxide semiconductor electrode," *Chem. Phys. Lett.*, vol. 183, no. 1&2, pp. 89–93, 1991.
- [95] G. Boschloo and D. Fitzmaurice, "Electron accumulation in nanostructured tio2 (anatase) electrodes," *J. Phys. Chem. B*, vol. 103, no. 37, pp. 7860–7868, 1999.
- [96] G. Redmond and D. Fitzmaurice, "Spectroscopic determination of flatband potentials for polycrystalline titania electrodes in nonaqueous solvents," *J. Phys. Chem.*, vol. 97, no. 7, pp. 1426–1430, 1993.
- [97] B. Enright, G. Redmond, and D. Fitzmaurice, "Spectroscopic determination of flatband potentials for polycrystalline tio2 electrodes in mixed solvent systems," *J. Phys. Chem.*, vol. 98, no. 24, pp. 6195–6200, 1994.
- [98] S. Rühle and D. Cahen, "Electron tunneling at the tio2/substrate interface can determine dye-sensitized solar cell performance," *J. Phys. Chem. B*, vol. 108, no. 46, pp. 17946–17951, 2004.
- [99] S. Ardo and G. J. Meyer, "Photodriven heterogeneous charge transfer with transition-metal compounds anchored to tio2 semiconductor surfaces," *Chem. Soc. Rev.*, vol. 38, no. 1, pp. 115–164, 2009.

- [100] K. Westermark, A. Henningsson, H. Rensmo, S. Södergren, H. Siegbahn, and A. Hagfeldt, "Determination of the electronic density of states at a nanostructured tio₂/ru-dye/electrolyte interface by means of photoelectron spectroscopy," *Chem. Phys.*, vol. 285, no. 1, pp. 157–165, 2002.
- [101] S. Rühle, M. Greenshtein, S. G. Chen, A. Merson, H. Pizem, C. S. Sukenik, D. Cahen, and A. Zaban, "Molecular adjustment of the electronic properties of nanoporous electrodes in dye-sensitized solar cells," *J. Phys. Chem. B*, vol. 109, no. 40, pp. 18907–18913, 2005.
- [102] S. G. Yan and J. T. Hupp, "Semiconductor-based interfacial electron-transfer reactivity: decoupling kinetics from ph-dependent band energetics in a dye-sensitized titanium dioxide/aqueous solution system," *J. Phys. Chem.*, vol. 100, no. 17, pp. 6867–6870, 1996.
- [103] M. Pastore and F. De Angelis, "Computational modelling of tio₂ surfaces sensitized by organic dyes with different anchoring groups: adsorption modes, electronic structure and implication for electron injection/recombination," *Phys. Chem. Chem. Phys.*, vol. 14, no. 2, pp. 920–928, 2012.
- [104] H. Kusama, H. Orita, and H. Sugihara, "Tio₂ band shift by nitrogen-containing heterocycles in dye-sensitized solar cells: a periodic density functional theory study," *Langmuir*, vol. 24, no. 8, pp. 4411–4419, 2008.
- [105] Y. Tachibana, S. A. Haque, I. P. Mercer, J. E. Moser, D. R. Klug, and J. R. Durrant, "Modulation of the rate of electron injection in dye-sensitized nanocrystalline tio₂ films by externally applied bias," *J. Phys. Chem. B*, vol. 105, no. 31, pp. 7424–7431, 2001.
- [106] P. Chen, J. H. Yum, F. De Angelis, E. Mosconi, S. Fantacci, S.-J. Moon, R. H. Baker, J. Ko, M. K. Nazeeruddin, and M. Grätzel, "High open-circuit voltage solid-state dye-sensitized solar cells with organic dye," *Nano Lett.*, vol. 9, no. 6, pp. 2487–2492, 2009.
- [107] M. Miyashita, K. Sunahara, T. Nishikawa, Y. Uemura, N. Koumura, K. Hara, A. Mori, T. Abe, E. Suzuki, and S. Mori, "Interfacial electron-transfer kinetics in metal-free organic dye-sensitized solar cells: Combined effects of molecular structure of dyes and electrolytes," *J. Am. Chem. Soc.*, vol. 130, no. 52, pp. 17874–17881, 2008.
- [108] L. Belpassi, I. Infante, F. Tarantelli, and L. Visscher, "The chemical bond between au(i) and the noble gases. comparative study of ngauf and ngau+ (ng = ar, kr, xe) by density functional and coupled cluster methods," *J. Am. Chem. Soc.*, vol. 130, no. 3, pp. 1048–1060, 2008.
- [109] G. te Velde, F. M. Bickelhaupt, E. J. Baerends, C. Fonseca Guerra, S. J. A. van Gisbergen, J. G. Snijders, and T. Ziegler, "Chemistry with adf," *J. Comput. Chem.*, vol. 22, no. 9, pp. 931–967, 2001.
- [110] M. Cossi, N. Rega, G. Scalmani, and V. Barone, "Energies, structures, and electronic properties of molecules in solution with the c-pcm solvation model," *J. Comput. Chem.*, vol. 24, no. 6, pp. 669–681, 2003.
- [111] M. J. Frisch, G. W. Trucks, H. B. Schlegel, G. E. Scuseria, M. A. Robb, J. R. Cheeseman, G. Scalmani, V. Barone, B. Mennucci, G. A. Petersson, H. Nakatsuji, M. Caricato, X. Li, H. P. Hratchian, A. F. Izmaylov, J. Bloino, G. Zheng, J. L. Sonnenberg, M. Hada, M. Ehara, K. Toyota, R. Fukuda, J. Hasegawa, M. Ishida, T. Nakajima, Y. Honda, O. Kitao, H. Nakai, T. Vreven, J. A. Montgomery, J. E. Peralta, F. Ogliaro, M. Bearpark, J. J. Heyd, E. Brothers, K. N. Kudin, V. N. Staroverov, R. Kobayashi, J. Normand, K. Raghavachari, A. Rendell, J. C. Burant, S. S. Iyengar, J. Tomasi, M. Cossi, N. Rega, J. M. Millam, M. Klene, J. E. Knox, J. B. Cross, V. Bakken, C. Adamo, J. Jaramillo, R. Gomperts, R. E. Stratmann, O. Yazyev, A. J. Austin, R. Cammi, C. Pomelli, J. W. Ochterski, R. L. Martin, K. Morokuma, V. G. Zakrzewski, G. A. Voth, P. Salvador, J. J. Dannenberg, S. Dapprich, A. D. Daniels, Farkas, J. B. Foresman, J. V. Ortiz, J. Cioslowski, and D. J. Fox, "Gaussian 09, revision a.02," 2009.

- [112] F. De Angelis, S. Fantacci, A. Selloni, M. K. Nazeeruddin, and M. Grätzel, “Time-dependent density functional theory investigations on the excited states of ru(ii)-dye-sensitized tio2 nanoparticles: The role of sensitizer protonation,” *J. Am. Chem. Soc.*, vol. 129, no. 46, pp. 14156–14157, 2007.
- [113] N. Martsinovich and A. Troisi, “Theoretical studies of dye-sensitised solar cells: from electronic structure to elementary processes,” *Energy Environ. Sci.*, vol. 4, pp. 4473–4495, 2011.
- [114] S. Agrawal, T. Leijtens, E. Ronca, M. Pastore, H. Snaith, and F. De Angelis, “Modeling the effect of ionic additives on the optical and electronic properties of a dye-sensitized tio2 heterointerface: absorption, charge injection and aggregation,” *J. Mater. Chem. A*, vol. 1, pp. 14675–14685, 2013.
- [115] T. Le Bahers, T. Pauporté, P. P. Lainé, F. Labat, C. Adamo, and I. Ciofini, “Modeling dye-sensitized solar cells: From theory to experiment,” *J. Phys. Chem. Lett.*, vol. 4, no. 6, pp. 1044–1050, 2013.
- [116] M. Pastore and F. De Angelis, *Modeling materials and processes in dye-sensitized solar cells: Understanding the mechanism, improving the efficiency*, pp. 151–236. Berlin, Heidelberg: Springer Berlin Heidelberg, 2014.
- [117] E. Mosconi, A. Selloni, and F. De Angelis, “Solvent effects on the adsorption geometry and electronic structure of dye-sensitized tio2: A first-principles investigation,” *J. Phys. Chem. C*, vol. 116, no. 9, pp. 5932–5940, 2012.
- [118] A. Monti, C. F. A. Negre, V. S. Batista, L. G. C. Rego, H. J. M. de Groot, and F. Buda, “Crucial role of nuclear dynamics for electron injection in a dye-semiconductor complex,” *J. Phys. Chem. Lett.*, vol. 6, no. 12, pp. 2393–2398, 2015.
- [119] M. Pastore, “First principle modelling of materials and processes in dye-sensitized photoanodes for solar energy and solar fuels,” *Computation*, vol. 5, no. 1, p. 5, 2017.
- [120] A. B. Munoz-Garcia and M. Pavone, “Structure and energy level alignment at the dye-electrode interface in p-type DSSCs: new hints on the role of anchoring modes from ab initio calculations,” *Phys. Chem. Chem. Phys.*, no. 3, pp. 12238–12246, 2015.
- [121] O. V. Kontkanen, M. Niskanen, T. I. Hukka, and T. T. Rantala, “Electronic structure of p-type perylene monoimide-based donor-acceptor dyes on the nickel oxide (100) surface: A dft approach,” *Phys. Chem. Chem. Phys.*, vol. 18, pp. 14382–14389, 2016.
- [122] M. Wykes, F. Odobel, C. Adamo, I. Ciofini, and F. Labat, “Anchoring groups for dyes in p-dssc application: Insights from dft,” *J. Mol. Model.*, vol. 22, no. 12, p. 289, 2016.
- [123] W. Wu, Z. Cao, and Y. Zhao, “Theoretical studies on absorption, emission, and resonance raman spectra of coumarin 343 isomers,” *J. Chem. Phys.*, vol. 136, no. 11, p. 114305, 2012.
- [124] R. J. Cave and E. W. Castner, “Time-dependent density functional theory investigation of the ground and excited states of coumarins 102, 152, 153, and 343,” *J. Phys. Chem. A*, vol. 106, no. 50, pp. 12117–12123, 2002.
- [125] P. Giannozzi, S. Baroni, N. Bonini, M. Calandra, R. Car, C. Cavazzoni, D. Ceresoli, G. L. Chiarotti, M. Cococcioni, I. Dabo, A. D. Corso, S. de Gironcoli, S. Fabris, G. Fratesi, R. Gebauer, U. Gerstmann, C. Gougoussis, A. Kokalj, M. Lazzeri, L. Martin-Samos, N. Marzari, F. Mauri, R. Mazzarello, S. Paolini, A. Pasquarello, L. Paulatto, C. Sbraccia, S. Scandolo, G. Sclauzero, A. P. Seitsonen, A. Smogunov, P. Umari, and R. M. Wentzcovitch, “Quantum espresso: a modular and open-source software project for quantum simulations of materials,” *J. Phys. Cond. Matt.*, vol. 21, no. 39, p. 395502, 2009.
- [126] M. Cococcioni and S. de Gironcoli, “Linear response approach to the calculation of the effective interaction parameters in the LDA+U method,” *Phys. Rev. B*, vol. 71, no. 3, p. 035105, 2005.

- [127] D. Vanderbilt, "Soft self-consistent pseudopotentials in a generalized eigenvalue formalism," *Phys. Rev. B*, vol. 41, p. 7892, 1990.
- [128] S. Grimme, "Semiempirical gga-type density functional constructed with a long-range dispersion correction," *J. Comp. Chem.*, vol. 27, no. 15, pp. 1787–1799, 2006.
- [129] C. S. Ponseca, P. Chábera, J. Uhlig, P. Persson, and V. Sundström, "Ultrafast electron dynamics in solar energy conversion," *Chem. Rev.*, vol. 117, no. 16, pp. 10940–11024, 2017.
- [130] A. Listorti, C. Creager, P. Sommeling, J. Kroon, E. Palomares, A. Fornelli, B. Breen, P. R. F. Barnes, J. R. Durrant, C. Law, and B. O'Regan, "The mechanism behind the beneficial effect of light soaking on injection efficiency and photocurrent in dye sensitized solar cells," *Energy Environ. Sci.*, vol. 4, no. 9, pp. 3494–3501, 2011.
- [131] A. Listorti, B. O'Regan, and J. R. Durrant, "Electron transfer dynamics in dye-sensitized solar cells," *Chem. Mater.*, vol. 23, no. 15, pp. 3381–3399, 2011.
- [132] N. A. Anderson and T. Lian, "Ultrafast electron transfer at the molecule-semiconductor nanoparticle interface," *Annu. Rev. Phys. Chem.*, vol. 56, no. 1, pp. 491–519, 2004.
- [133] M. G. Lobello, S. Fantacci, and F. De Angelis, "Computational spectroscopy characterization of the species involved in dye oxidation and regeneration processes in dye-sensitized solar cells," *J. Phys. Chem. C*, vol. 115, no. 38, pp. 18863–18872, 2011.
- [134] S. E. Koops, P. R. F. Barnes, B. C. O'Regan, and J. R. Durrant, "Kinetic competition in a coumarin dye-sensitized solar cell: Injection and recombination limitations upon device performance," *J. Phys. Chem. C*, vol. 114, no. 17, pp. 8054–8061, 2010.
- [135] S. Ferrere and B. A. Gregg, "Photosensitization of tio2 by [feii(2,2'-bipyridine-4,4'-dicarboxylic acid)2(cn)2]: Band selective electron injection from ultra-short-lived excited states," *J. Am. Chem. Soc.*, vol. 120, no. 4, pp. 843–844, 1998.
- [136] M. Yang, D. W. Thompson, and G. J. Meyer, "Dual pathways for tio2 sensitization by na2[fe(bpy)(cn)4]," *Inorg. Chem.*, vol. 39, no. 17, pp. 3738–3739, 2000. PMID: 11196762.
- [137] I. M. Dixon, F. Alary, M. Boggio-Pasqua, and J.-L. Heully, "Reversing the relative 3mlct-3mc order in fe(ii) complexes using cyclometallating ligands: a computational study aiming at luminescent fe(ii) complexes," *Dalton Trans.*, vol. 44, pp. 13498–13503, 2015.
- [138] T. Bessho, E. C. Constable, M. Graetzel, A. Hernandez Redondo, C. E. Housecroft, W. Kylberg, M. K. Nazeeruddin, M. Neuburger, and S. Schaffner, "An element of surprise-efficient copper-functionalized dye-sensitized solar cells," *Chem. Commun.*, pp. 3717–3719, 2008.
- [139] C. E. Housecroft and E. C. Constable, "The emergence of copper(i)-based dye sensitized solar cells," *Chem. Soc. Rev.*, vol. 44, pp. 8386–8398, 2015.
- [140] J. K. McCusker, K. N. Walda, R. C. Dunn, J. D. Simon, D. Magde, and D. N. Hendrickson, "Subpicosecond 1mlct .fwdarw. 5t2 intersystem crossing of low-spin polypyridyl ferrous complexes," *J. Am. Chem. Soc.*, vol. 115, no. 1, pp. 298–307, 1993.
- [141] J. E. Monat and J. K. McCusker, "Femtosecond excited-state dynamics of an iron(ii) polypyridyl solar cell sensitizer model," *Journal of the American Chemical Society*, vol. 122, no. 17, pp. 4092–4097, 2000.
- [142] M. Cammarata, R. Bertoni, M. Lorenc, H. Cailleau, S. Di Matteo, C. Mauriac, S. F. Matar, H. Lemke, M. Chollet, S. Ravy, C. Laulhé, J.-F. m. c. Létard, and E. Collet, "Sequential activation of molecular breathing and bending during spin-crossover photoswitching revealed by femtosecond optical and x-ray absorption spectroscopy," *Phys. Rev. Lett.*, vol. 113, p. 227402, Nov 2014.

- [143] B. E. Van Kuiken, H. Cho, K. Hong, M. Khalil, R. W. Schoenlein, T. K. Kim, and N. Huse, "Time-resolved x-ray spectroscopy in the water window: Elucidating transient valence charge distributions in an aqueous fe(ii) complex," *J. Phys. Chem. Lett.*, vol. 7, no. 3, pp. 465–470, 2016. PMID: 26727390.
- [144] Y. Liu, T. Harlang, S. E. Canton, P. Chabera, K. Suarez-Alcantara, A. Fleckhaus, D. A. Vithanage, E. Goransson, A. Corani, R. Lomoth, V. Sundstrom, and K. Wärnmark, "Towards longer-lived metal-to-ligand charge transfer states of iron(ii) complexes: an n-heterocyclic carbene approach," *Chem. Commun.*, vol. 49, pp. 6412–6414, 2013.
- [145] L. A. Fredin, M. Pápai, E. Rozsályi, G. Vankó, K. Wärnmark, V. Sundström, and P. Persson, "Exceptional excited-state lifetime of an iron(ii)-n-heterocyclic carbene complex explained," *J. Phys. Chem. Letters*, vol. 5, no. 12, pp. 2066–2071, 2014.
- [146] T. Duchanois, T. Etienne, M. Beley, X. Assfeld, E. A. Perpète, A. Monari, and P. C. Gros, "Heteroleptic pyridyl-carbene iron complexes with tuneable electronic properties," *Eu. J. Inorg. Chem.*, vol. 2014, no. 23, pp. 3747–3753, 2014.
- [147] T. C. B. Harlang, Y. Liu, O. Gordivska, L. A. Fredin, C. S. Ponceca Jr, P. Huang, P. Chábera, K. S. Kjaer, H. Mateos, J. Uhlig, R. Lomoth, R. Wallenberg, S. Styring, P. Persson, V. Sundström, and K. Wärnmark, "Iron sensitizer converts light to electrons with 92% yield," *Nat. Chem.*, vol. 7, pp. 883–889, 2015.
- [148] P. Zimmer, L. Burkhardt, A. Friedrich, J. Steube, A. Neuba, R. Schepper, P. Müller, U. Flörke, M. Huber, S. Lochbrunner, and M. Bauer, "The connection between nhc ligand count and photophysical properties in fe(ii) photosensitizers: An experimental study," *Inorg. Chem.*, vol. 57, no. 1, pp. 360–373, 2018.
- [149] P. Chábera, Y. Liu, O. Prakash, E. Thyrhaug, A. E. Nahhas, A. Honarfar, S. Essén, L. A. Fredin, T. C. B. Harlang, K. S. Kjær, K. Handrup, F. Ericson, H. Tatsuno, K. Morgan, J. Schnadt, L. Häggström, T. Ericsson, A. Sobkowiak, S. Lidin, P. Huang, S. Styring, J. Uhlig, J. Bendix, R. Lomoth, V. Sundström, P. Persson, and K. Wärnmark, "A low-spin fe(iii) complex with 100-ps ligand-to-metal charge transfer photoluminescence," *Nature*, vol. 543, pp. 695–699, 2017.
- [150] P. Chábera, K. S. Kjaer, O. Prakash, A. Honarfar, Y. Liu, L. A. Fredin, T. C. B. Harlang, S. Lidin, J. Uhlig, V. Sundström, R. Lomoth, P. Persson, and K. Wärnmark, "Feii hexa n-heterocyclic carbene complex with a 528 ps metal-to-ligand charge-transfer excited-state lifetime," *J. Phys. Chem. Lett.*, vol. 9, pp. 459–463, 2018.
- [151] H. Gerischer and F. Willig *Top. Curr. Chem.*, vol. 61, pp. 31–84, 1976. 978-3-540-07559-2.
- [152] H. Gerischer, "Electrochemical techniques for the study of photosensitization," *Photochem. Photobiol.*, vol. 16, no. 4, pp. 243–260, 1972. 1751-1097.
- [153] R. A. Marcus, "On the theory of electron-transfer reactions. vi. unified treatment for homogeneous and electrode reactions," *J. Chem. Phys.*, vol. 43, no. 2, pp. 679–701, 1965.
- [154] J. P. Muscat and D. M. Newns, "Chemisorption on metals," *Prog. Surf. Sci.*, vol. 9, no. 1, pp. 1–43, 1978.
- [155] C. Cohen-Tannoudji, B. Diu, and F. Laloe, *Quantum Mechanics*, vol. 2. Paris: J. Wiley & Sons, 1977.
- [156] P. Persson, M. J. Lundqvist, R. Ernstorfer, W. A. Goddard, and F. Willig, "Quantum chemical calculations of the influence of anchor-cum-spacer groups on femtosecond electron transfer times in dye-sensitized semiconductor nanocrystals," *J. Chem. Theory Comput.*, vol. 2, no. 2, pp. 441–451, 2006.
- [157] M. J. Lundqvist, M. Nilsing, S. Lunell, B. Åkermark, and P. Persson, "Spacer and anchor effects on the electronic coupling in ruthenium-bis-terpyridine dye-sensitized tio2 nanocrystals studied by dft," *J. Phys. Chem. B*, vol. 110, no. 41, pp. 20513–20525, 2006.

- [158] P. Persson and M. J. Lundqvist, “Calculated structural and electronic interactions of the ruthenium dye n3 with a titanium dioxide nanocrystal,” *J. Phys. Chem. B*, vol. 109, no. 24, pp. 11918–11924, 2005.
- [159] P. Persson, S. Lunell, and L. Ojamäe, “Quantum chemical prediction of the adsorption conformations and dynamics at hcooh-covered zno(1010) surfaces,” *Int. J. Quantum Chem.*, vol. 89, no. 3, pp. 172–180, 2002.
- [160] M. Pastore and F. De Angelis, “First-principles modeling of a dye-sensitized tio2/iro2 photoanode for water oxidation,” *J. Am. Chem. Soc.*, vol. 137, no. 17, pp. 5798–5809, 2015.
- [161] P. Umari, L. Giacomazzi, F. D. Angelis, M. Pastore, and S. Baroni, “Energy-level alignment in organic dye-sensitized tio2 from gw calculations,” *J. Chem. Phys.*, vol. 139, no. 1, p. 014709, 2013.
- [162] I. Kondov, M. Čížek, C. Benesch, H. Wang, and M. Thoss, “Quantum dynamics of photoinduced electron-transfer reactions in dye-semiconductor systems:a first-principles description and application to coumarin 343-tio2,” *J. Phys. Chem. C*, vol. 111, no. 32, pp. 11970–11981, 2007.
- [163] J. Li, H. Wang, P. Persson, and M. Thoss, “Photoinduced electron transfer processes in dye-semiconductor systems with different spacer groups,” *J. Chem. Phys.*, vol. 137, no. 22, p. 22A529–16, 2012.
- [164] A. Hagfeldt and L. Peter, *Dye-sensitized Solar Cells*. EPFL Press: Lausanne, 2010.
- [165] D. P. Hagberg, T. Marinado, K. M. Karlsson, K. Nonomura, P. Qin, G. Boschloo, T. Brinck, A. Hagfeldt, and L. Sun, “Tuning the homo and lumo energy levels of organic chromophores for dye sensitized solar cells,” *J. Org. Chem.*, vol. 72, no. 25, pp. 9550–9556, 2007.
- [166] M. Pastore, S. Fantacci, and F. De Angelis, “Ab initio determination of ground and excited state oxidation potentials of organic chromophores for dye-sensitized solar cells,” *J. Phys. Chem. C*, vol. 114, no. 51, pp. 22742–22750, 2010.
- [167] S. Kim, J. K. Lee, S. O. Kang, J. Ko, J. H. Yum, S. Fantacci, F. De Angelis, D. Di Censo, M. K. Nazeeruddin, and M. Grätzel, “Molecular engineering of organic sensitizers for solar cell applications,” *J. Am. Chem. Soc.*, vol. 128, no. 51, pp. 16701–16707, 2006.
- [168] M. Pastore and F. De Angelis, “Aggregation of organic dyes on tio2 in dye-sensitized solar cells models: An ab initio investigation,” *ACS Nano*, vol. 4, no. 1, pp. 556–562, 2010.
- [169] F. De Angelis, S. Fantacci, A. Selloni, M. K. Nazeeruddin, and M. Grätzel, “First-principles modeling of the adsorption geometry and electronic structure of ru(ii) dyes on extended tio2 substrates for dye-sensitized solar cell applications,” *J. Phys. Chem. C*, vol. 114, no. 13, pp. 6054–6061, 2010.
- [170] A. Vittadini, A. Selloni, F. P. Rotzinger, and M. Grätzel, “Structure and energetics of water adsorbed at tio2 anatase (101) and (001) surfaces,” *Phys. Rev. Lett.*, vol. 81, no. 14, pp. 2954–2957, 1998.
- [171] D. R. Jones and A. Troisi, “A method to rapidly predict the charge injection rate in dye sensitized solar cells,” *Phys. Chem. Chem. Phys.*, vol. 12, no. 18, pp. 4625–4634, 2010.
- [172] N. Martsinovich and A. Troisi, “High-throughput computational screening of chromophores for dye-sensitized solar cells,” *J. Phys. Chem. C*, vol. 115, no. 23, pp. 11781–11792, 2011.
- [173] J. Wiberg, T. Marinado, D. P. Hagberg, L. Sun, A. Hagfeldt, and B. Albinsson, “Effect of anchoring group on electron injection and recombination dynamics in organic dye-sensitized solar cells,” *J. Phys. Chem. C*, vol. 113, no. 9, pp. 3881–3886, 2009.
- [174] J. Wiberg, T. Marinado, D. P. Hagberg, L. Sun, A. Hagfeldt, and B. Albinsson, “Distance and driving force dependencies of electron injection and recombination dynamics in organic dye-sensitized solar cells,” *J. Phys. Chem. B*, vol. 114, no. 45, pp. 14358–14363, 2010.
- [175] J. Cioslowski, “A new population analysis based on atomic polar tensors,” *J. Am. Chem. Soc.*, vol. 111, no. 22, pp. 8333–8336, 1989.